SENSITIVITY-INFORMED IDENTIFICATION OF TEMPERATURE-DEPENDENT PIEZOELECTRIC MATERIAL PARAMETERS

RAPHAEL KUESS , OLGA FRIESEN , LEANDER CLAES , AND ANDREA WALTHER

Abstract. An accurate characterization of temperature-dependent material parameters of piezoceramics is crucial for the design and simulation of reliable sensors and actuators. This characterization is typically formulated as an ill-posed inverse problem, which is challenging to solve not only because of its ill-posedness, but also because of parameter sensitivities of the forward operator, which vary by several orders of magnitude and the strong coupling between parameters. For this reason, we propose a *block coordinate descent* (BCD) framework combined with a *globalized regularized structure-exploiting* (GRSE) Quasi-Newton method. A systematic sensitivity-driven strategy for the optimal partitioning of material parameters into blocks is established. By analyzing first- and second-order sensitivity information, our method identifies blocks that minimize inter-block coupling and group parameters with similar sensitivity profiles. Subsequent to a finite element discretization, the derivatives required for both the sensitivity analysis and the optimization are computed accurately using algorithmic differentiation. The proposed BCD-GRSE method is validated through a numerical experiment with noisy synthetic data. Finally, we present the reconstruction results for the piezoelectric material parameters of an annular sample based on physical measurement data.

Key words. inverse parameter identification, sensitivity analysis, piezoelectricity, block coordinate descent, regularized Quasi-Newton

MSC codes. 74J25, 90C31, 35R30, 49M15, 74M05

1. Introduction.

Piezoelectric components transform electrical energy into kinetic energy and vice versa and are therefore essential in a vast array of electronic devices, ranging from everyday items such as lighters and headphones to advanced medical and industrial applications like ultrasound imaging and ultrasonic bonding. Thoroughly understanding the behavior of these materials is crucial for designing high-performance devices, particularly given their temperature-dependent electromechanical characteristics. Piezoelectric ceramics undergo changes in behavior due to heating during operation, especially in high-power ultrasound applications, resulting in a resonance shift at which the device operates. Therefore, our aim is to develop a method for accurately predicting these changes to ensure device reliability and performance. Consequently, an optimization technique is required to determine the complete set of temperature-dependent material parameters (elastic, piezoelectric, and dielectric) from experimental measurements. This problem is formulated as an inverse problem, which is challenging for several reasons. It is ill-posed in the sense of Hadamard, i.e., the solution may not be unique or does not depend continuously on the data, necessitating regularization to ensure a stable and physically meaningful solution, see [20]. Furthermore, the problem is characterized by strong coupling and very different orders of magnitude between different material parameters. Additionally, the sensitivities of the forward operator with respect to different parameters vary by several orders of magnitude as well. To address these challenges, we propose an optimization framework based on a *Block Coordinate Descent* (BCD) strategy, where the parameters are partitioned based on a sensitivity and cross-sensitivity analysis. Within each block update, we employ the *regularized structure-exploiting Powell-Symmetric-Broyden* (RSE-PSB) method, see [19], that efficiently handles the remaining non-linearity and parameter coupling by incorporating second-order derivative approximations.

Related work. Common approaches to inverse material parameter identification problems in piezoelectricity involve minimizing the discrepancy between measured and simulated electrical impedance using Landweber or Gauss-Newton methods [14, 20]. A significant challenge arises due to the low sensitivity of the impedance to certain parameters. To enhance sensitivity, optimization of the geometry of the electrodes is investigated in [14]. The application of coordinate descent type methods to piezoelectric parameter identification was explored by [5, 7, 14]. These works address the known sensitivity issues of disc-shaped samples with electrodes fully covering both faces and propose a customized triple-ring electrode topology to increase the sensitivity. In [5], parameter updates are performed sequentially. In [7], certain parameters are optimized in frequency ranges where sensitivities are high only for that parameter. While effective to some extent, these approaches neglect parameter interactions that occur across different frequency bands. In the specific case of piezoceramic rings, it has been observed that the optimization of electrode topology is no longer necessary, as the sensitivity with respect to particular parameters is already increased by the given geometry compared to a piezoceramic disc [8], but the heterogeneity remains. The material parameters influenced by temperature were identified through the application of the above-mentioned methods in [9] and by implementing a neural network for initial estimates, followed by minimization of the data misfit as a final optimization step in [4]. Although satisfactory results have been achieved, the inverse problem was not considered from an analytical point of view, cross-sensitivities are only implicitly addressed. An algorithmic mechanism for dealing with the highly divergent sensitivities in the optimization routine and parameter coupling that fundamentally characterize this inverse problem has been barely discussed.

Contribution. In this paper, we develop a rigorous and practically applicable approach for identifying temperature-dependent piezoelectric material parameters using only a single ring-shaped sample. First, we analyze the inverse problem of identifying temperature-dependent piezoelectric parameters in the frequency domain. The analysis covers the well-posedness of the forward problem, Fréchet differentiability of the forward operator and the well-posedness of the continuous adjoint problem for all excitation frequencies. This provides the mathematical foundation for the discretize-then-optimize approach. Then, we propose a sensitivity-informed BCD framework for solving ill-posed inverse problems. Therein, we analyze first-order sensitivities, total sensitivities, cross-sensitivities, and a curvature-based intra-block roughness measure derived from second-order information. Based on these measures we present a systematic methodology to partition material parameters for the BCD algorithm into blocks, which uses first- and second-order sensitivity analysis to minimize the inter-block coupling (cross-sensitivity), while maintaining intra-block numerical stability (roughness). Subsequently, we combine the sensitivity-driven BCD framework with the RSE-PSB method and its globalized version (GRSE), which are analyzed from a theoretical perspective in [19]. The proposed BCD-GRSE algorithm, which is validated using synthetic noisy data, demonstrates its ability to accurately reconstruct all piezoelectric material parameters, even those with very low sensitivity. Finally, we present the reconstruction results for the material parameters of an annular PIC181 sample (*PI Ceramic, Germany*) with inner radius of 2.6 mm, outer radius of 6.35 mm and thickness of 1 mm, based on experimental measurement data across a temperature range of 25 °C – 85 °C. Using the reconstructed parameters, a substantial decrease in the data misfit is achieved, obtaining full temperature-dependent material descriptions from a single specimen.

Structure of the paper. Section 2 details the mathematical modeling, starting with the forward problem formulation and its analysis. The operators of the inverse problem are defined and the derivation and analysis of the continuous adjoint system follows. Section 3 presents the proposed numerical solution strategy. We introduce the RSE-PSB quasi-Newton method and embed it within the BCD framework. Next, the sensitivity-driven methodology for optimal block partitioning is discussed and the simulation-based inverse problem with synthetic data is solved in Section 4. Section 5 describes the experimental setup for measuring temperature-dependent impedance data and presents the results of applying our method to real-world measurements. Conclusions are given in Section 6.

2. Modeling and analysis of the inverse problem.

2.1. Modeling of the forward problem. For practical applications, thin, annular piezoelectric components with inner radius r_1, outer radius r_2, radial length $l = r_2 - r_1$ and height/thickness $h < l$, as illustrated in Figure 1, are the objects of high interest. We denote the geometry of the considered piezoceramic with a three-dimensional bounded domain $\Omega_{3\mathrm{d}} \subset \mathbb{R}^3$, i.e., $\Omega_{3\mathrm{d}}$ is a non-empty connected open subset of $\mathbb{R}^3$. The axisymmetric assumption allows a reduction of the computational complexity of the model from a three-dimensional (3D) to a two-dimensional (2D) problem, while capturing all relevant physical properties. Consequently, it is advantageous to utilize the symmetry of the geometry and to use the cylindrical instead of the Cartesian coordinate system. Hence, we obtain a rectangular Lipschitz domain $\Omega \subset \mathbb{R}^2$, where its boundary $\partial\Omega$ can be represented as the disjoint union $\partial\Omega := \Gamma_\mathrm{e} \dot\cup \Gamma_0 \dot\cup \Gamma_\mathrm{n}$. Here, Γ_e describes the boundary segment which is excited electrically with an excitation signal independent of the spatial domain (equally distributed) and Γ_0 refers to the boundary segment which is grounded. This can be modeled in the system of partial differential equations (PDEs) as Dirichlet boundary conditions. The segment Γ_n constitutes the remaining boundary of $\partial\Omega$ and is included in the PDE model by Neumann boundary conditions. Furthermore, we denote the non-empty mixed Dirichlet boundary with $\Gamma_\mathrm{d} := \Gamma_\mathrm{e} \dot\cup \Gamma_0$, i.e., $\partial\Omega := \Gamma_\mathrm{d} \dot\cup \Gamma_\mathrm{n}$. Assuming an initial stationary system, a macroscopic approach is adopted, where the constitutive laws in the so-called e-form read as

$$\sigma = c^\mathrm{E}(\theta) \cdot S - e(\theta) \cdot E, \quad D = e(\theta) \cdot S + \epsilon^\mathrm{S}(\theta) \cdot E,$$

and $\cdot$ denotes the inner product, σ the mechanical stress, S the mechanical strain, D the dielectric displacement and E the electric field. The material parameters $c^\mathrm{E}(\theta)$, $e(\theta)$ and $\epsilon^\mathrm{S}(\theta)$ contained therein are represented as temperature-dependent matrix-

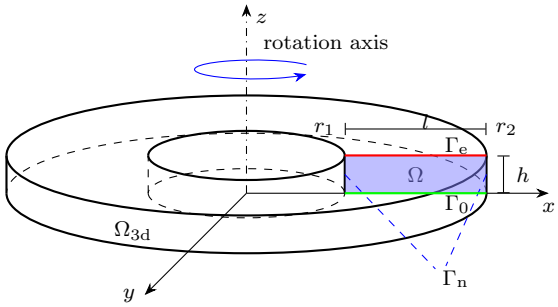


Figure 1: Geometric model of an annular piezoelectric specimen (3D domain $\Omega_{3\mathrm{d}}$) with its cross-section, i.e., 2D domain Ω derived from the axisymmetric domain $\Omega_{3\mathrm{d}}$.

valued functions that describe the material behavior of the piezoceramic under consideration. The superscripts E and S in the material parameters c^{E} and ϵ^{S} signal that these quantities are understood under conditions of constant electric field and constant mechanical strain, respectively. This approach offers valuable insights into the behavior of piezoelectric materials at varying temperatures, which are crucial in thermal coupling models. Given that temperatures are typically non-linear and continuous functions, non-linearity emerges at this point. Then, the constitutive laws are coupled to the equilibrium equations, namely Newton's second law of motion for mechanical behavior and Gauss's law, as well as to the field equations, i.e., Faraday's law and the displacement gradient, where we consider the differential operators

$$\nabla := \begin{pmatrix} \frac{\partial}{\partial r} \\ \frac{\partial}{\partial z} \end{pmatrix} \quad \text{and} \quad \mathcal{B} = \begin{pmatrix} \frac{\partial}{\partial r} & \frac{1}{r} & 0 & \frac{\partial}{\partial z} \\ 0 & 0 & \frac{\partial}{\partial z} & \frac{\partial}{\partial r} \end{pmatrix}^{\mathrm{T}}$$

in Voigt notation transformed to cylindrical coordinates. We denote the normal vector corresponding to ∇ with n and the normal element corresponding to $\mathcal{B}$ with $\mathcal{N}$. In order to model the physical behavior more reliably, it is necessary to include a damping model. In this context, we assume only the occurrence of mechanical friction for which a simplified model, namely the Rayleigh damping model, is employed in the mechanical equation, introducing the mass-proportional and stiffness-proportional damping parameters α and β. This is a common simplification to describe energy dissipation within the material during elastic processes [6]. Furthermore, we assume that the piezoceramic is initially at rest, i.e., the piezoelectric specimen is not vibrating, stretched or compressed. Since measurement data depending on the state are frequently observed in frequency domain, we consider a Fourier transformation of the transient system in [18] with space and time constant damping and material parameters. Hence, we obtain the harmonic PDE

$$\begin{aligned}
\forall \omega \in \mathcal{W}: \quad -\rho\omega^2 s_1 \hat{u} - \mathcal{B}^{\mathrm{T}} \left(s_2 c^{\mathrm{E}}(\theta) \mathcal{B}\hat{u} + e(\theta)^{\mathrm{T}} \nabla \hat{\phi} \right) &= 0 \quad \text{in } \Omega \\
-\nabla \cdot \left(e(\theta)\mathcal{B}\hat{u} - \epsilon^{\mathrm{S}}(\theta)\nabla\hat{\phi} \right) &= 0 \quad \text{in } \Omega \\
\hat{\phi} &= 0 \quad \text{on } \Gamma_0 \\
\hat{\phi} &= \hat{\phi}^{\mathrm{e}} \quad \text{on } \Gamma_{\mathrm{e}} \\
n \cdot \left(e(\theta)\mathcal{B}\hat{u} - \epsilon^{\mathrm{S}}(\theta)\nabla\hat{\phi} \right) &= 0 \quad \text{on } \Gamma_{\mathrm{n}} \\
\mathcal{N}^{\mathrm{T}} \left(s_2 c^{\mathrm{E}}(\theta)\mathcal{B}\hat{u} + e(\theta)^{\mathrm{T}}\nabla\hat{\phi} \right) &= 0 \quad \text{on } \partial\Omega,
\end{aligned}$$

where i is the imaginary unit, $s_1 := 1 - \mathrm{i}\frac{\alpha}{\omega}$, $s_2 := 1 + \mathrm{i}\omega\beta$ and $\alpha, \beta \in \mathbb{R}^+$. Note that this approach does not use the additional assumption of multiplying α and dividing β by ω, as in [20]. Furthermore, $\rho \in \mathbb{R}^+$ is the mass density and $\phi^{\mathrm{e}} \in H^1(0,T)$ is a known excitation function. We denoted the space of angular frequencies with $\mathcal{W} \subset \mathbb{R}^+$, $|\mathcal{W}| < \infty$, where $\omega = 2\pi f$ is the angular frequency and $f \in \mathcal{F} \subset \mathbb{R}^+$ is the frequency. This formulation is also computationally advantageous as it allows us to solve a series of smaller, independent problems rather than a single large time-dependent one. The parameters $c^{\mathrm{E}}(\theta), e(\theta)$, and $\epsilon^{\mathrm{S}}(\theta)$ are defined as follows.

DEFINITION 2.1 (Material parameter functions). *Let $\Theta \subset \mathbb{R}^+$ be a bounded temperature domain and $\eta \in \mathbb{R}^+$. Then, the elasticity parameter*

$$c^{\mathrm{E}}(\theta) := \begin{pmatrix} c_{11}(\theta) & c_{12}(\theta) & c_{13}(\theta) & 0 \\ c_{12}(\theta) & c_{11}(\theta) & c_{13}(\theta) & 0 \\ c_{13}(\theta) & c_{13}(\theta) & c_{33}(\theta) & 0 \\ 0 & 0 & 0 & c_{44}(\theta) \end{pmatrix}$$

is a matrix-valued function, where c_{12} and c_{13} are positive functions,

$$c_{11}(\theta) > \eta + c_{12}(\theta), \quad c_{44}(\theta) > \eta, \quad c_{33}(\theta) > c_{13}(\theta) + \eta, \quad c_{11}(\theta) + c_{12}(\theta) \geq 2c_{13}(\theta)$$

and $c_{11}, c_{12}, c_{13}, c_{33}, c_{44} \in L^2(\Theta, \mathbb{R})$, the piezoelectric coupling parameter

$$e(\theta) := \begin{pmatrix} 0 & 0 & 0 & e_{15}(\theta) \\ e_{31}(\theta) & e_{31}(\theta) & e_{33}(\theta) & 0 \end{pmatrix}$$

with $e_{15}, e_{31}, e_{33} \in L^2(\Theta, \mathbb{R})$ is a matrix-valued function and the permittivity parameter

$$\epsilon^{\mathrm{S}}(\theta) := \begin{pmatrix} \epsilon_{11}(\theta) & 0 \\ 0 & \epsilon_{33}(\theta) \end{pmatrix},$$

is a matrix-valued function, where $\epsilon_{11}(\theta) > \eta, \quad \epsilon_{33}(\theta) > \eta$ and $\epsilon_{11}, \epsilon_{33} \in L^2(\Theta, \mathbb{R})$.

LEMMA 2.2. *The material parameters $c^{\mathrm{E}}(\theta)$ and $\epsilon^{\mathrm{S}}(\theta)$ defined in Definition 2.1 are uniformly invertible with bounded inverse.*

Proof. For $c^{\mathrm{E}}(\theta)$ we compute the eigenvalues

$$\lambda_1(\theta) = c_{44}(\theta), \ \lambda_2(\theta) = c_{11}(\theta) - c_{12}(\theta),$$

$$\lambda_3(\theta) = \frac{1}{2}\left(c_{11}(\theta) + c_{12}(\theta) + c_{33}(\theta) - \sqrt{8(c_{13}(\theta))^2 + (c_{11}(\theta) + c_{12}(\theta) - c_{33}(\theta))^2}\right),$$

$$\lambda_4(\theta) = \frac{1}{2}\left(c_{11}(\theta) + c_{12}(\theta) + c_{33}(\theta) + \sqrt{8(c_{13}(\theta))^2 + (c_{11}(\theta) + c_{12}(\theta) - c_{33}(\theta))^2}\right).$$

Hence $\lambda_1(\theta), \lambda_2(\theta) > \eta$. Furthermore, it holds that

$$\lambda_4(\theta) > \frac{1}{2}\left(c_{11}(\theta) + c_{12}(\theta) + c_{33}(\theta)\right) > \frac{\eta + \eta}{2} = \eta.$$

As $c_{11}(\theta) + c_{12}(\theta) \geq 2c_{13}(\theta)$, one has $1 \geq \frac{2c_{13}(\theta)}{c_{11}(\theta)+c_{12}(\theta)}$, which yields

$$c_{33}(\theta) > c_{13}(\theta) + \eta \geq \frac{2(c_{13}(\theta))^2}{c_{11}(\theta) + c_{12}(\theta)} + \eta. \tag{2.1}$$

To bound $\lambda_3(\theta)$, we define a function $g(x)$ by substituting x for $c_{33}(\theta)$ in the eigenvalue $\lambda_3(\theta)$, i.e., viewing λ_3 as a smooth function of $c_{33}(\theta)$. Differentiating g yields

$$g'(x) = \frac{1}{2}\left(1 + \frac{c_{11}(\theta) + c_{12}(\theta) - x}{\sqrt{(c_{11}(\theta) + c_{12}(\theta) - x)^2 + 8(c_{13}(\theta))^2}}\right) > 0.$$

Hence, g is a strictly increasing function on $\mathbb{R}$, as the fractional term is strictly bounded between -1 and 1. We deduce that $\lambda_3(\theta) = g(c_{33}(\theta)) > g\left(\frac{2(c_{13}(\theta))^2}{c_{11}(\theta)+c_{12}(\theta)} + \eta\right)$

by monotonicity using $c_{33}(\theta) > \frac{2(c_{13}(\theta))^2}{c_{11}(\theta)+c_{12}(\theta)} + \eta$. Consequently, we obtain

$$\lambda_3(\theta) > \frac{1}{2}\left(c_{11}(\theta) + c_{12}(\theta) + \frac{2(c_{13}(\theta))^2}{c_{11}(\theta)+c_{12}(\theta)} + \eta \right.$$
$$\left. - \sqrt{\frac{\left((c_{11}(\theta))^2 + 2c_{11}(\theta)c_{12}(\theta) + (c_{12}(\theta))^2 + 2(c_{13}(\theta))^2\right)^2}{(c_{11}(\theta)+c_{12}(\theta))^2}}\right) = \frac{\eta}{2},$$

where we used inequality (2.1). Hence, $c^{\mathrm{E}}(\theta)$ has eigenvalues bounded away from 0. The conditions for $\epsilon^{\mathrm{S}}(\theta)$ are obvious. ∎

Consequently, the conditions in Definition 2.1 can be seen as sufficient conditions to obtain physical stability of the material, as they ensure that the strain energy density is positive definite. Hence, we define the parameter space

$$X := \Big\{ p \in L^2(\Theta, \mathbb{R})^{10} : \ p_1 = c_{11},\ p_2 = c_{12},\ p_3 = c_{13},\ p_4 = c_{33},\ p_5 = c_{44},$$
$$p_6 = \epsilon_{11},\ p_7 = \epsilon_{33},\ p_8 = e_{15},\ p_9 = e_{31},\ p_{10} = e_{33} \Big\}. \tag{2.2}$$

For our function space setting, we consider

$$H^1_{\mathcal{B}}(\Omega, \mathbb{C}^2) := \left\{ u \in L^2(\Omega, \mathbb{C}^2) \,\middle|\, \|u\|_{H^1_{\mathcal{B}}(\Omega,\mathbb{C}^2)} := \|u\|_{L^2(\Omega,\mathbb{C}^2)} + \|\mathcal{B}u\|_{L^2(\Omega,\mathbb{C}^4)} < \infty \right\}$$

and

$$H^2_{0,\Gamma}(\Omega, \mathbb{C}) = \left\{ g \in H^2(\Omega, \mathbb{C}) \mid g|_{(\Gamma_{\mathrm{e}} \cup \Gamma_0)} = 0 \right\},$$
$$H^2_{\mathcal{B}}(\Omega, \mathbb{C}^2) = \left\{ g \in L^2(\Omega, \mathbb{C}^2) \mid \|g\|_{H^2_{\mathcal{B}}(\Omega,\mathbb{C}^2)} < \infty \right\},$$

where $\|g\|_{H^2_{\mathcal{B}}(\Omega,\mathbb{C}^2)} := \|g\|_{L^2(\Omega,\mathbb{C}^2)} + \|\mathcal{B}g\|_{L^2(\Omega,\mathbb{C}^2)} + \left\|\mathcal{B}^{\mathrm{T}}\mathcal{B}g\right\|_{L^2(\Omega,\mathbb{C}^2)}$. The choice of these Sobolev spaces is motivated by the structure of the weak formulation. The spaces $H^2(\Omega)$ and $H^2_{\mathcal{B}}(\Omega, \mathbb{C}^2)$ provide sufficient regularity for the observation operator to be well-defined, see [18]. To discuss the operators of the inverse problem, we homogenize the mixed Dirichlet boundary conditions using the Dirichlet lift Ansatz, which is particularly convenient to prove well-posedness of the forward problem. By similar arguments as in Remark 3.5 in [18] there exists a $\chi \in H^2(\Omega, \mathbb{C})$ satisfying

$$\mathrm{Tr}(\chi) = \begin{cases} \hat{\phi}^{\mathrm{e}} & \text{on } \Gamma_{\mathrm{e}} \\ 0 & \text{on } \Gamma_0 \end{cases} \tag{2.3}$$

and a $\hat{\phi}_0 \in H^2_{0,\Gamma}(\Omega, \mathbb{C})$, such that $\hat{\phi} = \hat{\phi}_0 + \chi$. Hence, the harmonic PDE simplifies to

$$-\rho\omega^2 s_1 \hat{u} - \mathcal{B}^{\mathrm{T}}\left(s_2 c^{\mathrm{E}}(\theta)\mathcal{B}\hat{u} + e(\theta)^{\mathrm{T}}\nabla\hat{\phi}_0\right) = \mathcal{B}^{\mathrm{T}} e(\theta)^{\mathrm{T}}\nabla\chi \qquad \text{in } \Omega \tag{2.4}$$

$$-\nabla\cdot\left(e(\theta)\mathcal{B}\hat{u} - \epsilon^{\mathrm{S}}(\theta)\nabla\hat{\phi}_0\right) = -\nabla\cdot\epsilon^{\mathrm{S}}(\theta)\nabla\chi \quad \text{in } \Omega \tag{2.5}$$

$$n\cdot\left(e(\theta)\mathcal{B}\hat{u} - \epsilon^{\mathrm{S}}(\theta)\nabla\hat{\phi}_0\right) = n\cdot\epsilon^{\mathrm{S}}(\theta)\nabla\chi \qquad \text{on } \Gamma_{\mathrm{n}} \tag{2.6}$$

$$\mathcal{N}^{\mathrm{T}}\left(s_2 c^{\mathrm{E}}(\theta)\mathcal{B}\hat{u} + e(\theta)^{\mathrm{T}}\nabla\hat{\phi}_0\right) = -\mathcal{N}^{\mathrm{T}} e(\theta)^{\mathrm{T}}\nabla\chi \quad \text{on } \partial\Omega \tag{2.7}$$

for all $\omega \in \mathcal{W}$, where $(\hat{u}, \hat{\phi}_0) \in H^2_{\mathcal{B}}(\Omega, \mathbb{C}^2) \times H^2_{0,\Gamma}(\Omega, \mathbb{C})$ is the weak solution of the system above. Since we used a coordinate transformation, the weak form is given by

$$2\pi \int_\Omega \Big(-s_1 \rho \omega^2 \hat{u}^{\mathrm{T}} \overline{v} + \Big(s_2 c^{\mathrm{E}}(\theta) \mathcal{B}\hat{u} + e(\theta)^{\mathrm{T}} \nabla \hat{\phi}_0 \Big)^{\mathrm{T}} \overline{\mathcal{B}v} + \Big(e(\theta)\mathcal{B}\hat{u}$$

$$-\epsilon^{\mathrm{S}}(\theta)\nabla\hat{\phi}_0\Big)^{\mathrm{T}} \overline{\nabla w} \Big) \, r \, \mathrm{d}\Omega = 2\pi \int_\Omega \left(-(e(\theta)^{\mathrm{T}} \nabla \chi)^{\mathrm{T}} \overline{\mathcal{B}v} + (\epsilon^{\mathrm{S}}(\theta)\nabla\chi)^{\mathrm{T}} \overline{\nabla w} \right) r \, \mathrm{d}\Omega \tag{2.8}$$

for suitable test functions (v, w) belonging to the solution space, where the radius

$$r \in C^\infty(\overline{\Omega}, \mathbb{R}) \text{ satisfies } \; 0 < r_1 \le r(x) \le r_2 < \infty \quad \text{a.e. in } \Omega. \tag{2.9}$$

THEOREM 2.3. *Let $\Omega \subset \mathbb{R}^2$ be a convex Lipschitz domain, $\chi \in H^2(\Omega, \mathbb{C})$ satisfying* (2.3) *and $\theta \in \Theta$ be fixed. Let the material parameters be defined as in Definition 2.1, the radius as in* (2.9) *and $\rho, \alpha, \beta \in \mathbb{R}^+$. Then, there exists a unique solution to* (2.8)*, i.e., a unique weak solution*

$$(\hat{u}, \hat{\phi}_0) \in H^2_{\mathcal{B}}(\Omega, \mathbb{C}^2) \times H^2_{0,\Gamma}(\Omega, \mathbb{C}) \tag{2.10}$$

to the system (2.4) - (2.7)*, where $s_1 := 1 - \mathrm{i}\frac{\alpha}{\omega}$, $s_2 := 1 + \mathrm{i}\omega\beta$. Furthermore, there exists a constant $c = C(\omega, r_1, r_2, c^{\mathrm{E}}, e, \epsilon^{\mathrm{S}}, \rho, \alpha, \beta) > 0$ such that*

$$\|(\hat{u}, \hat{\phi}_0)\|_{H^1_{\mathcal{B}}(\Omega,\mathbb{C}^2) \times H^1_{0,\Gamma}(\Omega,\mathbb{C})} \le c \|\chi\|_{H^2(\Omega,\mathbb{C})}.$$

Proof. First, we define $V := H^1_{\mathcal{B}}(\Omega, \mathbb{C})^2 \times H^1_{0,\Gamma}(\Omega, \mathbb{C})$ and prove the existence of a unique weak solution $(\hat{u}, \hat{\phi}_0) \in V$ to the system (2.4) - (2.7). For this purpose, we use test functions $(v, w) \in V$ and obtain the weak form as in (2.8), where we want to find $(\hat{u}, \hat{\phi}_0) \in V$ such that $a_\omega((\hat{u}, \hat{\phi}_0), (v, w)) = f_\omega(v, w)$ for all $(v, w) \in V$, where

$$a_\omega((\hat{u}, \hat{\phi}_0), (v, w)) = 2\pi \int_\Omega \Big(-s_1 \rho \omega^2 \hat{u}^{\mathrm{T}} \overline{v} + \Big(s_2 c^{\mathrm{E}}(\theta) \mathcal{B}\hat{u} + e(\theta)^{\mathrm{T}} \nabla \hat{\phi}_0 \Big)^{\mathrm{T}} \overline{\mathcal{B}v}$$

$$+ \Big(e(\theta)\mathcal{B}\hat{u} - \epsilon^{\mathrm{S}}(\theta)\nabla\hat{\phi}_0 \Big)^{\mathrm{T}} \overline{\nabla w} \Big) \, r \, \mathrm{d}\Omega$$

and

$$f_\omega(v, w) = 2\pi \int_\Omega \left(-(e(\theta)^{\mathrm{T}} \nabla \chi)^{\mathrm{T}} \overline{\mathcal{B}v} + (\epsilon^{\mathrm{S}}(\theta)\nabla\chi)^{\mathrm{T}} \overline{\nabla w} \right) r \, \mathrm{d}\Omega \, .$$

Since $e(\theta)$ and $\epsilon^{\mathrm{S}}(\theta)$ are constant matrices, $r \in C^\infty(\overline{\Omega})$ is bounded and $\chi \in H^2(\Omega, \mathbb{C})$, applying Hölder's inequality to f_ω yields that there exists $c_1 > 0$ such that

$$|f_\omega(v, w)| \le c_1 \|\chi\|_{H^2(\Omega)} \|(v, w)\|_V .$$

Thus, f_ω is continuous on V. Similarly, using the boundedness of the material parameters and the radius, as well as Hölder's inequality, we obtain that a_ω is continuous on V. We decompose the bilinear form into a principal a_0 and a term a_k such that $a_\omega = a_0 + a_k$, where

$$a_0((\hat{u}, \hat{\phi}_0), (v, w)) := 2\pi \int_\Omega \Big(\hat{u}^{\mathrm{T}} \overline{v} + s_2 (\mathcal{B}\hat{u})^{\mathrm{T}} c^{\mathrm{E}}(\theta) \overline{\mathcal{B}v} + (\nabla \hat{\phi}_0)^{\mathrm{T}} e(\theta) \overline{\mathcal{B}v}$$

$$+ (\mathcal{B}\hat{u})^{\mathrm{T}} e(\theta)^{\mathrm{T}} \overline{\nabla w} - (\nabla \hat{\phi}_0)^{\mathrm{T}} \epsilon^{\mathrm{S}}(\theta) \overline{\nabla w} \Big) r \, \mathrm{d}\Omega \, ,$$

$$a_k((\hat{u}, \hat{\phi}_0), (v, w)) := 2\pi \int_\Omega - \left(s_1 \rho \omega^2 \hat{u}^{\mathrm{T}} \overline{v} + \hat{u}^{\mathrm{T}} \overline{v} \right) \, r \, \mathrm{d}\Omega \, .$$

We identify the operator $\mathcal{A}_0 : V \to V^*$ induced by a_0 via

$$\mathcal{A}_0 : V \to V^*, \quad \langle \mathcal{A}_0(u,\phi),(v,w)\rangle = a_0((u,\phi),(v,w)).$$

To prove that $\mathcal{A}_0$ is an isomorphism we define the modified bilinear form

$$b((\hat{u},\hat{\phi}_0),(v,w)) := a_0((\hat{u},\hat{\phi}_0),(v,-w)). \tag{2.11}$$

Evaluating $b((\hat{u},\hat{\phi}_0),(\hat{u},\hat{\phi}_0))$ yields

$$\begin{aligned} b\big((\hat{u},\hat{\phi}_0),(\hat{u},\hat{\phi}_0)\big) = 2\pi \int_\Omega \Big(&\hat{u}^{\mathrm{T}}\overline{\hat{u}} + s_2(\mathcal{B}\hat{u})^{\mathrm{T}} c^{\mathrm{E}}(\theta)\,\overline{\mathcal{B}\hat{u}} + (\nabla\hat{\phi}_0)^{\mathrm{T}} e(\theta)\,\overline{\mathcal{B}\hat{u}} \\ &- (\mathcal{B}\hat{u})^{\mathrm{T}} e(\theta)^{\mathrm{T}}\,\overline{\nabla\hat{\phi}_0} + (\nabla\hat{\phi}_0)^{\mathrm{T}}\epsilon^{\mathrm{S}}(\theta)\,\overline{\nabla\hat{\phi}_0}\Big)\, r\,\mathrm{d}\Omega. \end{aligned}$$

We observe that the coupling terms satisfy

$$(\mathcal{B}\hat{u})^{\mathrm{T}} e(\theta)^{\mathrm{T}}\,\overline{\nabla\hat{\phi}_0} = \overline{(\nabla\hat{\phi}_0)^{\mathrm{T}} e(\theta)\,\overline{\mathcal{B}\hat{u}}}.$$

Consequently, they are complex conjugates with opposite sign, meaning their sum is purely imaginary. As $\mathrm{Re}(s_2) = \mathrm{Re}(1+\mathrm{i}\omega\beta) = 1$, we obtain

$$\mathrm{Re}\, b((\hat{u},\hat{\phi}_0),(\hat{u},\hat{\phi}_0)) = 2\pi\int_\Omega \Big(|\hat{u}|^2 + (\mathcal{B}\hat{u})^{\mathrm{T}} c^{\mathrm{E}}(\theta)\overline{\mathcal{B}\hat{u}} + (\nabla\hat{\phi}_0)^{\mathrm{T}}\epsilon^{\mathrm{S}}(\theta)\overline{\nabla\hat{\phi}_0}\Big)\, r\,\mathrm{d}\Omega.$$

Since $c^{\mathrm{E}}(\theta)$ and $\epsilon^{\mathrm{S}}(\theta)$ are uniformly positive definite and $r \geq r_1 > 0$ a.e. in Ω, there exists $\tilde{c} > 0$ such that

$$\mathrm{Re}\, b\big((\hat{u},\hat{\phi}_0),(\hat{u},\hat{\phi}_0)\big) \geq 2\pi r_1 \tilde{c}\int_\Omega \Big(|\hat{u}|^2 + |\mathcal{B}\hat{u}|^2 + |\nabla\hat{\phi}_0|^2\Big)\,\mathrm{d}\Omega \geq c_2 \|(\hat{u},\hat{\phi}_0)\|_V^2$$

for some $c_2 > 0$, where we used the definition of $H^1_{\mathcal{B}}(\Omega,\mathbb{C}^2)$ and Poincaré's inequality. Thus, b is strictly coercive. By the Lax-Milgram theorem, b induces an isomorphism from V to V^*. Since the mapping $\mathcal{T} : V \to V$, defined by $\mathcal{T}(v,w) = (v,-w)$, is an isomorphism and $a_0((\hat{u},\hat{\phi}_0),(v,w)) = b((\hat{u},\hat{\phi}_0),\mathcal{T}(v,w))$, it follows that $\mathcal{A}_0$ is an isomorphism. Since $r \geq r_1 > 0$, the definition of $\mathcal{B}$ yields $\|\mathcal{B}u\|_{L^2(\Omega,\mathbb{C}^4)} \leq C(r_1)\|u\|_{H^1(\Omega,\mathbb{C}^2)}$ with a constant $C(r_1) > 0$ depending only on r_1. Conversely, since the components of the symmetric gradient are contained in $\mathcal{B}u$, Korn's inequality gives $\|u\|_{H^1(\Omega,\mathbb{C}^2)} \leq C\left(\|u\|_{L^2(\Omega,\mathbb{C}^2)} + \|\mathcal{B}u\|_{L^2(\Omega,\mathbb{C}^4)}\right)$. Hence, the $H^1_{\mathcal{B}}(\Omega,\mathbb{C}^2)$-norm is equivalent to the standard $H^1(\Omega,\mathbb{C}^2)$-norm. Moreover, it holds that $H^1_{0,\Gamma}(\Omega,\mathbb{C}) \subset H^1(\Omega,\mathbb{C})$. Since Ω is a bounded Lipschitz domain, the Rellich-Kondrachov theorem yields the compact embedding $V \hookrightarrow L^2(\Omega,\mathbb{C}^2)\times L^2(\Omega,\mathbb{C})$. The operator $\mathcal{A}_k : V \to V^*$ induced by a_k can be explicitly factored through the space $H := L^2(\Omega,\mathbb{C}^2)\times L^2(\Omega,\mathbb{C})$. Specifically $\mathcal{A}_k$ can be factored through the Gelfand triple $V \hookrightarrow H \cong H^* \hookrightarrow V^*$, as $\mathcal{A}_k$ is the composition of the compact embedding $i : V \hookrightarrow H$, the (bounded) multiplication operator and the (bounded) dual embedding $i^* : H \to V^*$, where H is identified with its dual H^* via the Riesz representation theorem. Consequently, the operator $\mathcal{A}_k : V \to V^*$ is compact, yielding $\mathcal{A}_\omega = \mathcal{A}_0 + \mathcal{A}_k$ to be a compact perturbation of an isomorphism, i.e., a Fredholm operator of index zero. To show injectivity, we assume that $(\hat{u},\hat{\phi}_0) \in V$ satisfies $\mathcal{A}_\omega(\hat{u},\hat{\phi}_0) = 0$. Using $s_1 := 1 - \mathrm{i}\frac{\alpha}{\omega}$ and testing with $(\hat{u},\hat{\phi}_0)$, one obtains

$$\mathrm{Im}\left(a_\omega((\hat{u},\hat{\phi}_0),(\hat{u},\hat{\phi}_0))\right) = 2\pi\int_\Omega \Big(\frac{\alpha}{\omega}\rho\omega^2|\hat{u}|^2 + \omega\beta(\mathcal{B}\hat{u})^{\mathrm{T}} c^{\mathrm{E}}(\theta)\overline{\mathcal{B}\hat{u}}\Big) r\,\mathrm{d}\Omega = 0.$$

Since the radius is bounded away from zero and $\alpha, \beta > 0$, one has $\hat{u} = 0$ and $\mathcal{B}\hat{u} = 0$. Substituting $\hat{u} = 0$ back into $a_\omega((\hat{u}, \hat{\phi}_0), (v, w)) = 0$ and choosing $w = -\hat{\phi}_0$ yields

$$\int_\Omega (\nabla \hat{\phi}_0)^{\mathrm{T}} \epsilon^{\mathrm{S}}(\theta) \overline{\nabla \hat{\phi}_0}\, r \, \mathrm{d}\Omega = 0,$$

and hence $\nabla \hat{\phi}_0 = 0$. Since $\hat{\phi}_0 \in H^1_{0,\Gamma}(\Omega)$, Poincaré's inequality implies $\hat{\phi}_0 = 0$. Thus, the kernel is trivial, yielding injectivity of $\mathcal{A}_\omega$. Since $\mathcal{A}_\omega$ is a Fredholm operator of index zero, it is bijective, and therefore admits a unique weak solution $(\hat{u}, \hat{\phi}_0) \in V$. Consequently, there exists a constant $c = C(\omega, r_1, r_2, c^{\mathrm{E}}, e, \epsilon^{\mathrm{S}}, \rho, \alpha, \beta) > 0$ such that

$$\|(\hat{u}, \hat{\phi}_0)\|_{H^1_{\mathcal{B}}(\Omega,\mathbb{C}^2)\times H^1_{0,\Gamma}(\Omega,\mathbb{C})} \leq c \|\chi\|_{H^2(\Omega)}.$$

Second, we lift the solution to H^2-regularity. For this purpose, we will use a bootstrap argument. Denoting the unique weak solution as $(\hat{u}^\dagger, \hat{\phi}_0^\dagger) \in V$, we rewrite the system (2.4) - (2.5) as $\mathcal{L}_\omega z = g$, where $z = (\hat{u}, \hat{\phi}_0)^{\mathrm{T}}$,

$$\mathcal{L}_\omega z = \begin{pmatrix} -\mathcal{B}^{\mathrm{T}} \left(s_2 c^{\mathrm{E}}(\theta) \mathcal{B}\hat{u} + e(\theta)^{\mathrm{T}} \nabla \hat{\phi}_0 \right) \\ -\nabla \cdot \left(e(\theta) \mathcal{B}\hat{u} - \epsilon^{\mathrm{S}}(\theta) \nabla \hat{\phi}_0 \right) \end{pmatrix}, \quad g = \begin{pmatrix} \rho\omega^2 s_1 \hat{u}^\dagger + \mathcal{B}^{\mathrm{T}} e(\theta)^{\mathrm{T}} \nabla \chi \\ -\nabla \cdot \epsilon^{\mathrm{S}}(\theta) \nabla \chi \end{pmatrix}.$$

Due to the relative signs in the electrostatic part, $\mathcal{L}_\omega$ represents a saddle-point problem. To overcome this drawback, we multiply the second equation (2.5) by -1, defining the equivalent system $\tilde{\mathcal{L}}_\omega z = \tilde{g}$, whose derivative terms coincide with those of the bilinear form b defined in (2.11). As the bilinear form b is strictly coercive on V, Theorem 4.6 in [22] implies that the differential operator associated with b is strongly elliptic. Since this operator differs from $\tilde{\mathcal{L}}_\omega$ only by the added zeroth-order term, the corresponding differential operator $\tilde{\mathcal{L}}_\omega$ is strongly elliptic as well. Since $\chi \in H^2(\Omega, \mathbb{C})$ and $\rho\omega^2 s_1 \hat{u}^\dagger \in H^1_{\mathcal{B}}(\Omega, \mathbb{C}^2)$, the total right-hand side data $\tilde{g}$ belongs to $L^2(\Omega, \mathbb{C}^2) \times L^2(\Omega, \mathbb{C})$. The goal is now to apply the elliptic regularity argument for convex domains of Theorem 3.2.1.3 in [12]. The spatially constant material parameters and $r \in C^\infty(\overline{\Omega})$ with $r \geq r_1 > 0$ ensure that the coefficients of the differential operator are bounded. Furthermore, Ω is a convex Lipschitz domain and the homogeneous Dirichlet condition is incorporated in the state space. The remaining boundary conditions are the natural ones associated with the weak formulation. By the preceding argument, $\tilde{\mathcal{L}}_\omega$ is strongly elliptic and $\tilde{g} \in L^2(\Omega, \mathbb{C}^2) \times L^2(\Omega, \mathbb{C})$. Consequently, the elliptic regularity argument of Theorem 3.2.1.3 carries over component wise to the present finite-dimensional strongly elliptic system. Hence, the weak solution to $\tilde{\mathcal{L}}_\omega z = \tilde{g}$ attains H^2 regularity. Because $\tilde{\mathcal{L}}_\omega z = \tilde{g}$ is equivalent to the original system $\mathcal{L}_\omega z = g$, this higher regularity applies directly to our original problem. Since $r \in C^\infty(\overline{\Omega})$ and $r \geq r_1 > 0$, $\hat{u} \in H^2(\Omega, \mathbb{C}^2)$ implies $\mathcal{B}\hat{u} \in H^1(\Omega, \mathbb{C}^4)$ and $\mathcal{B}^{\mathrm{T}}\mathcal{B}\hat{u} \in L^2(\Omega, \mathbb{C}^2)$. Therefore, one has $\hat{u} \in H^2_{\mathcal{B}}(\Omega, \mathbb{C}^2)$. Moreover, $\hat{\phi}_0 \in H^2(\Omega, \mathbb{C})$ together with $\hat{\phi}_0 \in H^1_{0,\Gamma}(\Omega, \mathbb{C})$ yields $\hat{\phi}_0 \in H^2_{0,\Gamma}(\Omega, \mathbb{C})$. By the uniqueness of the weak solution in V, the unique solution $(\hat{u}, \hat{\phi}_0)$ belongs to $H^2_{\mathcal{B}}(\Omega, \mathbb{C}^2) \times H^2_{0,\Gamma}(\Omega, \mathbb{C})$. ∎

2.2. Operators of the inverse problem. To formulate the inverse problem, we discretize the continuous temperature dependency and denote the discretized temperature interval of finite cardinality as $\Theta \subset \mathbb{R}^+$. Since $|\Theta| < \infty$, the space $L^2(\Theta, \mathbb{R})^{10}$ equipped with the counting measure is canonically isomorphic to $\mathbb{R}^{10N}$,

where $N = |\Theta|$. Consequently, the parameter space for each $\theta \in \Theta$ is given by

$$X_\theta := \Big\{ p \in \mathbb{R}^{10} : \; p_1 = c_{11},\; p_2 = c_{12},\; p_3 = c_{13},\; p_4 = c_{33},\; p_5 = c_{44}, \\ p_6 = \epsilon_{11},\; p_7 = \epsilon_{33},\; p_8 = e_{15},\; p_9 = e_{31},\; p_{10} = e_{33} \Big\}. \tag{2.12}$$

This allows us to solve the inverse problem for the material parameters at each discrete temperature point $\theta \in \Theta$. For this purpose, we employ the state space

$$W := \left(H^2_{\mathcal{B}}(\Omega, \mathbb{C}^2) \times H^2_{0,\Gamma}(\Omega, \mathbb{C}) \right)^{|\mathcal{W}|},$$

which coincides with the solution space of the system (2.4) - (2.7). This reflects that for a given parameter p, the forward problem consists of solving the harmonic PDE for each angular frequency $\omega \in \mathcal{W}$ independently. Therefore, a single state $z \in W$ is a collection of solutions $z = \{z_\omega\}_{\omega \in \mathcal{W}}$ with $z_\omega = (\hat{u}_\omega, \hat{\phi}_{0,\omega})$. Then the model operator will be defined as follows.

DEFINITION 2.4 (Model operator). *The piezoelectric model operator $A^\theta : X_\theta \times W \to W^*$ is defined for a fixed temperature $\theta \in \Theta$ via the weak form* (2.8) *component wise for each $\omega \in \mathcal{W}$, i.e., it is given by*

$$\langle A^\theta_\omega(p,z), (v,w) \rangle_{W^*,W} := 2\pi \int_\Omega \Big(- s_1 \rho \omega^2 \hat{u}^{\mathrm{T}} \overline{v} + \Big(s_2 c^{\mathrm{E}}(\theta) \mathcal{B}\hat{u} + e^{\mathrm{T}}(\theta) \nabla \hat{\phi}_0 \Big)^{\mathrm{T}} \overline{\mathcal{B}v} \\ + \Big(e(\theta)\mathcal{B}\hat{u} - \epsilon^{\mathrm{S}}(\theta) \nabla \hat{\phi}_0 \Big)^{\mathrm{T}} \overline{\nabla w} + (e^{\mathrm{T}}(\theta) \nabla \hat{\chi})^{\mathrm{T}} \overline{\mathcal{B}v} - (\epsilon^{\mathrm{S}}(\theta) \nabla \hat{\chi})^{\mathrm{T}} \overline{\nabla w} \Big) r \, \mathrm{d}\Omega \,,$$

where we abbreviated $z = (\hat{u}, \hat{\phi}_0)$.

To recover information on the parameter p, we need observations of the state z and the parameter. Hence, we define the measured charge pulse, where the electrodes are conductive and thus the charge is distributed equally on the loaded electrode.

DEFINITION 2.5 (Observation operator). *The measured charge pulse for a fixed temperature $\theta \in \Theta$ is defined component wise for each $\omega \in \mathcal{W}$ by*

$$Q^\theta_\omega(p,z) = 2\pi \int_{\Gamma_{\mathrm{e}}} r \left(e(\theta)\mathcal{B}\hat{u} - \epsilon^{\mathrm{S}}(\theta) \nabla \left(\hat{\phi}_0 + \hat{\chi} \right) \right) \cdot n \, \mathrm{d}\Gamma \,. \tag{2.13}$$

Motivated by physical observations, we assume that $\left\| Q^\theta_\omega(p,z) \right\|_{\mathbb{C}} > 0$ for all $(p,z) \in X_\theta \times W$ and define the observation operator $C^\theta : X_\theta \times W \to \mathbb{R}^{|\mathcal{W}|}$ for a fixed temperature $\theta \in \Theta$ component wise for each $\omega \in \mathcal{W}$ as

$$C^\theta_\omega(p,z) = \log \left(\left\| Q^\theta_\omega(p,z) \right\|_{\mathbb{C}} \right). \tag{2.14}$$

The logarithm is applied to the measured quantity to handle the large dynamic range of the electrical charge pulse, which can vary by several orders of magnitude, especially near resonance and anti-resonance frequencies. To model the inverse problem, we employ the reduced approach, meaning that we have to eliminate the model by introducing a so-called parameter-to-state map, which maps the parameter to the weak solution of the underlying PDE model (2.4) - (2.7).

DEFINITION 2.6 (Parameter-to-state map). *The parameter-to-state map for a fixed temperature* $\theta \in \Theta$

$$\mathcal{S}^\theta : X_\theta \to W, \qquad p \mapsto z,$$

is defined by satisfying the model stated in Definition 2.4, i.e.,

$$\forall z \in W : \ [(p,z) \in X_\theta \times W \ \wedge \ \langle A^\theta(p,z), \zeta\rangle = 0 \ \forall \zeta \in W] \implies z = \mathcal{S}^\theta(p),$$

where ζ *denotes the test function.*

THEOREM 2.7. *For each* $\theta \in \Theta$ *it holds that the operator* A^θ *introduced in Definition 2.4 is well-defined, bounded, bijective and continuously Fréchet differentiable on* $X_\theta \times W$*, the operator* C^θ *given in Definition 2.5 is well-defined, bounded and continuously Fréchet differentiable on* $X_\theta \times W$ *and the operator* $\mathcal{S}^\theta$ *introduced in Definition 2.6 is well-defined, non-linear and continuously Fréchet differentiable on* X_θ*.*

Proof. Bijectivity and well-definedness of A^θ for each $\theta \in \Theta$ are consequences of Theorem 2.3. Analogous arguments as in the proof of Lemma 4.5 in [18] yield continuous Fréchet differentiability of A^θ with respect to both the parameters and the state for each temperature $\theta \in \Theta$. Following the same strategy, we obtain that $\mathcal{S}^\theta$ is well-defined and continuously Fréchet differentiable on X_θ for each temperature $\theta \in \Theta$. The non-linearity of $\mathcal{S}^\theta$ can be obtained from the structure of the model operator. Lastly, using Theorem 2.3 and analogous arguments as in the proof of Remark 4.6 in [18] with $m = 2$ for each $\theta \in \Theta$ implies that the operator Q^θ defined in (2.13) is well-defined, bounded and continuously Fréchet differentiable on $X_\theta \times W$ for each temperature $\theta \in \Theta$. As $\left\|Q^\theta_\omega(p,z)\right\|_{\mathbb{C}} > 0$ for each $\omega \in \mathcal{W}$ and the logarithm is smooth on $\mathbb{R}^+$, we deduce that C^θ defined in (2.14) is well-defined, bounded, non-linear and continuously Fréchet differentiable on $X_\theta \times W$ for each temperature. ∎

Note that the spatial H^2-regularity of solutions to the piezoelectric system are needed in time-domain as well as in frequency-domain formulations, since the observation operator contains a boundary integral of spatial derivatives of this solution. Using the same arguments, one can immediately conclude the forward operator is even twice continuously Fréchet differentiable.

2.3. The resulting inverse problem and adjoint system. Since observations are usually contaminated with noise up to a noise level δ, we have given the positive noisy data $\tilde{y}^\delta_\theta \in \mathbb{R}^{|\mathcal{W}|}$, which we transform component wise logarithmically

$$y^\delta_\theta := \log\left(\tilde{y}^\delta_\theta\right).$$

For the forward operator for each fixed temperature $\theta \in \Theta$

$$F^\theta : X_\theta \to \mathbb{R}^{|\mathcal{W}|}, \quad F^\theta(p) = C^\theta(p, \mathcal{S}^\theta(p)),$$

we want to identify $p \in X_\theta$ such that

$$F^\theta(p) = y^\delta_\theta. \tag{2.15}$$

Hence, the reduced approach casts the problem into an operator equation in $\mathbb{R}^{|\mathcal{W}|}$ for the sought-after quantity p. This problem is ill-posed in the sense of Hadamard, see [20], meaning the solution may not be unique or may not depend continuously on the data. Small perturbations in the measurement data y^δ_θ can lead to large

deviations in the reconstructed parameter function p. Regularization is therefore essential to stabilize the solution process. Consequently, we introduce a weakly lower semicontinuous regularizer $\mathcal{R}_\tau : X_\theta \to \mathbb{R}$ with a regularization parameter $\tau > 0$. Then, we model the inverse problem similarly to [20] as an optimization problem, where we aim at finding a minimizer of the regularized target functional $\mathcal{J} : X_\theta \to \mathbb{R}$,

$$\mathcal{J}(p) := J_\theta(p) + \mathcal{R}_\tau(p) \quad \text{with} \quad J_\theta(p) := \frac{1}{2}\left\|F^\theta(p) - y_\theta^\delta\right\|^2_{\mathbb{R}^{|\mathcal{W}|}} \tag{2.16}$$

for each fixed $\theta \in \Theta$, which we assume to exist. Using derivative-based methods necessitates gradient computation, which is often done via adjoints. Hence, unique existence of the adjoint state is desirable, as it can be seen as revealing the influence of a cause on a target functional. To obtain the adjoint system to (2.4) - (2.7), we differentiate A_ω^θ with respect to the state in the direction (d, ψ) for each $\theta \in \Theta$

$$\begin{aligned}\frac{\mathrm{d}A((\hat{u},\hat{\phi}_0),(v,w))}{\mathrm{d}\left(\hat{u},\hat{\phi}_0\right)}(d,\psi) &= \frac{\partial A((\hat{u},\hat{\phi}_0),(v,w))}{\partial \hat{u}}d + \frac{\partial A((\hat{u},\hat{\phi}_0),(v,w))}{\partial \hat{\phi}_0}\psi \\ &= 2\pi\int_\Omega \Big(-s_1\rho\omega^2 d^{\mathrm{T}}\overline{v} + \left(s_2 c^{\mathrm{E}}(\theta)\mathcal{B}d + e(\theta)^{\mathrm{T}}\nabla\psi\right)^{\mathrm{T}}\overline{\mathcal{B}v} \\ &\quad + \left(e(\theta)\mathcal{B}d - \epsilon^{\mathrm{S}}(\theta)\nabla\psi\right)^{\mathrm{T}}\overline{\nabla w}\Big)\, r\,\mathrm{d}\Omega\,.\end{aligned} \tag{2.17}$$

We introduce the corresponding parameter- and state-dependent analogue of J_θ in (2.16),

$$\widehat{J}_\theta(p,z) := \frac{1}{2}\left\|C_\omega^\theta(p,z) - y_\theta^\delta\right\|^2_{\mathbb{R}^{|\mathcal{W}|}}, \qquad J_\theta(p) = \widehat{J}_\theta\big(p, \mathcal{S}^\theta(p)\big)$$

and its the derivative with respect to $(\hat{u},\hat{\phi}_0)$ for each $\omega \in \mathcal{W}$

$$\frac{\mathrm{d}\widehat{J}_{\theta,\omega}(p,z)}{\mathrm{d}\left(\hat{u},\hat{\phi}_0\right)}(d,\psi) = \left(C_\omega^\theta(p,(\hat{u},\hat{\phi}_0)) - y_{\theta,\omega}^\delta\right)\frac{\mathrm{d}C_\omega^\theta(p,(\hat{u},\hat{\phi}_0))}{\mathrm{d}\left(\hat{u},\hat{\phi}_0\right)}(d,\psi).$$

As the regularizer depends only on p, it does not contribute to the derivative with respect to the state. Since $C_\omega^\theta(p,(\hat{u},\hat{\phi}_0)) = \log\left(\left\|Q_\omega^\theta(p,(\hat{u},\hat{\phi}_0))\right\|_{\mathbb{C}}\right)$, we obtain

$$\begin{aligned}\frac{\mathrm{d}C_\omega^\theta(p,(\hat{u},\hat{\phi}_0))}{\mathrm{d}\left(\hat{u},\hat{\phi}_0\right)}(d,\psi) &= \frac{\mathrm{Re}\left(\overline{Q_\omega^\theta(p,(\hat{u},\hat{\phi}_0))}\dfrac{\mathrm{d}Q_\omega^\theta(p,(\hat{u},\hat{\phi}_0))}{\mathrm{d}\left(\hat{u},\hat{\phi}_0\right)}(d,\psi)\right)}{\left\|Q_\omega^\theta(p,(\hat{u},\hat{\phi}_0))\right\|^2_{\mathbb{C}}}, \\ \frac{\mathrm{d}Q_\omega^\theta(p,(\hat{u},\hat{\phi}_0))}{\mathrm{d}\left(\hat{u},\hat{\phi}_0\right)}(d,\psi) &= 2\pi\int_{\Gamma_{\mathrm{e}}} r\left(e(\theta)\mathcal{B}d - \epsilon^{\mathrm{S}}(\theta)\nabla\psi\right)\cdot n\,\mathrm{d}\Gamma.\end{aligned}$$

Accordingly, the negative state derivative of the data-misfit functional defines the right-hand sides of the adjoint system by

$$
\begin{aligned}
f_\omega^\theta(p,(\hat{u},\hat{\phi}_0)) &:= -\left(\frac{\mathrm{d}C_\omega^\theta(p,(\hat{u},\hat{\phi}_0))}{\mathrm{d}\hat{u}}\right)^* \left(C_\omega^\theta(p,(\hat{u},\hat{\phi}_0)) - y_{\theta,\omega}^\delta\right), \\
g_\omega^\theta(p,(\hat{u},\hat{\phi}_0)) &:= -\left(\frac{\mathrm{d}C_\omega^\theta(p,(\hat{u},\hat{\phi}_0))}{\mathrm{d}\hat{\phi}_0}\right)^* \left(C_\omega^\theta(p,(\hat{u},\hat{\phi}_0)) - y_{\theta,\omega}^\delta\right),
\end{aligned} \tag{2.18}
$$

where * represents the Hilbert-space adjoint. Denoting the adjoint state as $(q_1, q_2) \in H^2_{\mathcal{B}}(\Omega,\mathbb{C}^2) \times H^2_{0,\Gamma}(\Omega,\mathbb{C})$ and partially integrating the derivative (2.17) yields the adjoint system

$$
\forall \omega \in \mathcal{W}: \quad -\rho\omega^2 s_1 \overline{q_1} - \mathcal{B}^{\mathrm{T}}\left(s_2 c^{\mathrm{E}}(\theta)\mathcal{B}\overline{q_1} + e(\theta)^{\mathrm{T}}\nabla\overline{q_2}\right) = f_\omega^\theta(p,(\hat{u},\hat{\phi}_0)) \quad \text{in } \Omega \tag{2.19}
$$

$$
-\nabla\cdot\left(e(\theta)\mathcal{B}\overline{q_1} - \epsilon^{\mathrm{S}}(\theta)\nabla\overline{q_2}\right) = g_\omega^\theta(p,(\hat{u},\hat{\phi}_0)) \quad \text{in } \Omega \tag{2.20}
$$

$$
n\cdot\left(e(\theta)\mathcal{B}\overline{q_1} - \epsilon^{\mathrm{S}}(\theta)\nabla\overline{q_2}\right) = 0 \quad \text{on } \Gamma_n \tag{2.21}
$$

$$
\mathcal{N}^{\mathrm{T}}\left(s_2 c^{\mathrm{E}}(\theta)\mathcal{B}\overline{q_1} + e(\theta)^{\mathrm{T}}\nabla\overline{q_2}\right) = 0 \quad \text{on } \partial\Omega, \tag{2.22}
$$

which is uniquely solvable for every state $(\hat{u},\hat{\phi}_0) \in W$ due to Theorem 2.3. As we want to employ *algorithmic differentiation* (AD) in a *discretize-then-optimize* (DO) approach for the actual calculation of the adjoint and hence, the gradient, well-posedness of the continuous adjoint problem, including the existence and uniqueness of the adjoint state, serves as an essential mathematical foundation. Consequently, the analysis of the continuous problem (2.19) - (2.22) is an important prerequisite for AD and the DO approach, since the frequently used reverse mode of AD is related to solving the discrete adjoint corresponding to the forward problem [3].

3. The BCD RSE-QN approach. In practical solution approaches to inverse problems in piezoelectricity, sensitivities of the forward operator with respect to different parameters vary considerably, see [15]. For a better handling of sensitivities we propose a *block coordinate descent* (BCD) method. BCD methods are usually iterative methods in which the minimization of the objective functional with respect to a previously selected block consisting of components of the optimization variables is achieved in each iteration step, while the remaining components of the optimization variables are fixed to their values of the current iteration, see [26]. This block is then updated and fixed for the next block. On the one hand, the advantage is that each of these sub-problems is lower-dimensional than the original minimization problem and, on the other hand, regarding second-order methods, the degrees of freedom in the corresponding Hessian operators (or approximations thereof) are reduced, see [26]. To illustrate the approach, let $X \subset \mathbb{R}^n$ and choose for the optimization problem

$$
\min_{p\in X} \mathcal{J}(p) \tag{3.1}
$$

a block B_i^k containing coordinates with indices $b_i^k \subseteq \{1,2,\dots,n\}$, where k refers to the k-th iteration step and i to the block used in the k-th iteration step. Then, we update the corresponding sub-vector $p^{b_i^k} \in \mathbb{R}^{|b_i^k|}$ of the optimization variables, i.e.,

$$
p_{k+1}^{b_i^k} = p_k^{b_i^k} + s_k,
$$

where $s_k \in \mathbb{R}^{|b_i^k|}$ is typically a descent direction of the lower dimensional sub-problem. With $I_{b_i^k}$ denoting the $|b_i^k| \times |b_i^k|$ dimensional identity matrix embedded in $\mathbb{R}^{n\times|b_i^k|}$, we can reformulate the BCD update as

$$p^{k+1} = p^k + I_{b_i^k} s_k,$$

see [24]. The next block B_{i+1}^k is chosen according to $b_{i+1}^k \subseteq \{1,2,\dots,n\} \setminus \cup_{l=1}^{i} b_l^k$. There are different ways to realize the BCD method, and therefore to define the block B_i^k as well as the direction s_k. Firstly, we need a strategy to select an appropriate b_i^k. Possibilities for this choice would be to fix certain disjoint partitions of $\{1,2,\dots,n\}$ with a prescribed cardinality a-priori. This means that we cycle through the same partitions every time, which is known as cyclic selection and refers to the Gauss-Seidel method for linear systems. Next, one could choose the block size and the coordinates therein in each iteration, which is called variable block selection. Therefore, blocks can be chosen from all possible subsets of $\{1,2,\dots,n\}$ randomly or with greedy approaches, where an underlying optimization problem must be solved to obtain the optimal block. If the iteration costs are high, then greedy BCD versions are too costly. Furthermore, [24] suggests using fixed blocks over variable blocks, Newton-type methods for each block as well as larger and fewer blocks if the iteration cost does not increase heavily. Since, e.g., [14], also recommends to apply Newton-type methods in the context of parameter identification problems in piezoelectricity, we will use the RSE-PSB method, see [19]. This can be seen as a "corrected" *Levenberg-Marquardt* (LM) method or a regularized structure-exploiting *Quasi-Newton* (QN) method especially designed for solving inverse problems, where second order derivative information is desirable because of non-linearity or cross-sensitivity information. Consequently, the regularizer in (2.16) is chosen as Tikhonov-type regularizer

$$\mathcal{R}_{\tau_k} : X \to \mathbb{R}^+,\ p \mapsto \frac{\tau_k}{2}\|p - p_k\|_X^2 \tag{3.2}$$

iteration-wise. By computing the Hessian of $\mathcal{J}$ defined in (2.16) at the point p_k using the regularizer defined in (3.2), i.e.,

$$H(p_k) := F'(p_k)^* F'(p_k) + F''(p_k)^* \left(F(p_k) - y^\delta\right) + \tau_k I,$$

where the first derivative of the regularizer in (3.2) vanishes at p_k, while its second derivative is $\tau_k I$, one obtains the regularized Newton method

$$H(p_k)(p_{k+1} - p_k) = F'(p_k)^* \left(y^\delta - F(p_k)\right),$$

where we omit the superscript corresponding to the temperature for the sake of readability. Computing H directly is numerically very costly and using the LM method, i.e., $A_k = 0$ for all $k \in \mathbb{N}$, inherits an approximation error that is only small if F is linear or the residual is sufficiently small. Hence, the idea is to use QN methods, but those methods often do not take the structure of $\mathcal{J}$ and H into account. Therefore, if we assume that F' is known or easily accessible, analogously to the LM method, only

$$Z(p_k) := F''(p_k)^* \left(F(p_k) - y^\delta\right)$$

is difficult and expensive to compute. Therefore, the idea of the RSE-PSB method is to minimize the data-misfit functional via employing QN updates for A_k such that $A_k \approx Z(p_k)$. Note that even the specific QN method has to be chosen carefully, as

Z may not be positive definite, while still symmetric. Consequently, we define the residual $r_k := F(p_k) - y^\delta$ and the step $s_k := p_{k+1} - p_k$. A Taylor approximation leads to the modified secant condition,

$$(F''(p_k)^* r_k) s_k = (F'(p_{k+1}) - F'(p_k))^* r_{k+1}, \text{ and } y_k := (F'(p_{k+1}) - F'(p_k))^* r_{k+1}.$$

Then, we obtain the PSB update to approximate $F''(p_k)^* r_k$ via

$$A_{k+1} = A_k + \frac{(y_k - A_k s_k) \otimes s_k + s_k \otimes (y_k - A_k s_k)}{\langle s_k, s_k \rangle} - \frac{\langle y_k - A_k s_k, s_k \rangle s_k \otimes s_k}{\langle s_k, s_k \rangle^2},$$

where $\otimes$ denotes the outer product. Using the PSB update for computing A_k and

$$\mathcal{B}_k := F'(p_k)^* F'(p_k) + A_k + \tau_k I$$

as approximation operator to $H(p_k)$ yields the RSE-PSB method, which is given by

$$\mathcal{B}_k(p_{k+1} - p_k) = F'(p_k)^* \left(y^\delta - F(p_k)\right).$$

To ensure the regularization property as well as robustness in practical applications, particularly when the initial guess significantly deviates from the true solution, and to have a concrete choice of the regularization parameter, [19] adapted an approach from [16]. The idea is to control the regularization parameter such that it leads to globalization. Therefore, the control approach also serves as an a-priori rule to choose the regularization parameter. This strategy yields a globalization technique, ensuring convergence towards a local minimizer even when the initial guess p_0 is far from the true solution, while simultaneously regularizing the inverse problem [19]. We combine this QN approach with a cyclic BCD method. Therefore, the blocks do not change during the optimization process, i.e., $b_i^k = b_i$. We denote $m < n$ as the number of blocks and $\dot{\cup}_{i=1}^m b_i = \{1, 2, \ldots, n\}$. The resulting BCD-GRSE algorithm is shown in Algorithm 3.1. For this purpose, we denote $p_k := (p_k^1, \cdots, p_k^m)$ corresponding to the blocks $b_1, \cdots, b_m$. Conditioning the decrease of the regularization parameters on the first occurrence of convergence in the preceding blocks can enhance stability in practical applications.

Remark 3.1. The convergence results in [19] do not apply immediately to the cyclic BCD-GRSE method, since the block updates are performed successively at intermediate iterates and each block has its own QN approximation and regularization parameter. However, the assumptions in [19] admit natural blockwise analogues, under which the corresponding convergence arguments can be adapted to obtain finite termination of the blockwise regularization loops, convergence of the block gradients to zero for vanishing block gradient thresholds and finite termination for positive block gradient thresholds.

An open question is which parameters should be grouped together in one block. Thus, we want to tackle the problem of coordinate choice and having highly heterogeneous sensitivity values by a sensitivity driven partitioning approach. For this purpose, we analyze the sensitivities and cross-sensitivities. The sensitivity of a quantity measures the change in this quantity when certain influences (parameters) change. The cross-sensitivity measures the potential for mutual influence between two specific parameters in relation to changes in a specific quantity. Both measures can be understood as first-order (sensitivity) and second-order (cross-sensitivity) derivatives. Note that sensitivities may also be defined differently, e.g., via second-order difference

Algorithm 3.1 BCD-GRSE algorithm

Require: $k = 0; c, a, \mu \in (0,1); \sigma > 1; p_0 \in \mathbb{R}^n; y^\delta \in \mathbb{R}^{|\mathcal{W}|}; b_i \subseteq \{1, 2, \ldots, n\} \setminus \cup_{l=1}^{i-1} b_l;$
$A_0^i \in \mathbb{R}^{|b_i|\times|b_i|}; \tau_0^i > 0; g_0^i > \eta^i, i = 1, \cdots, m.$
while $g_k^j > \eta^j$ for at least one $j = 1, \cdots, m$ **do**
for $i = 1, \cdots, m$ **do**
Evaluate $F(p_k)$, compute $F'_{b_i}(p_k)$, $r_k = F(p_k) - y^\delta$, $J'_{b_i}(p_k) = F'_{b_i}(p_k)^* r_k$.
if $k > 0$: **then**
Set $\check{p}_k \leftarrow (p_k^1, \cdots, p_k^{i-1}, p_{k-1}^i, p_k^{i+1}, \cdots p_k^m)$, compute $F'_{b_i}(\check{p}_k)$ and A_k^i with PSB.
end if
if eq. (3.3) is solvable: **then** Compute s_k as solution of

$$\left(F'_{b_i}(p_k)^* F'_{b_i}(p_k) + A_k^i + \tau_k^i I\right) s_k = -J'_{b_i}(p_k). \tag{3.3}$$

Compute
$\text{pred}_k = \frac{\tau_k^i}{2}\|s_k\|^2 - \frac{1}{2} J'_{b_i}(p_k)^T s_k$, $\text{ared}_k = J_{b_i}(p_k) - J_{b_i}(p_k + s_k)$, $\rho_k = \frac{\text{ared}_k}{\text{pred}_k}$.
elseSet $\rho_k = \text{pred}_k = s_k = 0$.
end if
while $\rho_k \le c$ or $\text{pred}_k \le a g_k^i \|s_k\|$: **do**
if eq. (3.3) is not solvable **then**
Set $\tau_k^i \leftarrow \sigma \tau_k^i$
else
Set $\tau_k^i \leftarrow \sigma \tau_k^i$ and solve eq. (3.3) for s_k and compute
$\text{pred}_k = \frac{\tau_k^i}{2}\|s_k\|^2 - \frac{1}{2} J'_{b_i}(p_k)^T s_k$, $\text{ared}_k = J_{b_i}(p_k) - J_{b_i}(p_k + s_k)$, $\rho_k = \frac{\text{ared}_k}{\text{pred}_k}$.
end if
end while
Update $\hat{p}_k^i \leftarrow p_k^i + s_k$ and $p_k \leftarrow (\hat{p}_k^1, \cdots, \hat{p}_k^{i-1}, \hat{p}_k^i, p_k^{i+1}, \cdots p_k^m)$
Set $\tau_{k+1}^i \leftarrow \mu \tau_k^i$ and compute $g_{k+1}^i = \left\|J'_{b_i}(p_k)\right\|$
end for
Update $p_{k+1} \leftarrow (\hat{p}_k^1, \cdots, \hat{p}_k^m)$ and $k = k + 1$
end while

quotients [7], Sobol's method [2], or statistically through conditional expectations and variances [21]. As parameters may have different physical units and magnitudes, normalized parameters x_i, satisfying $p_i = x_i \|p_i\|$, are used to reformulate $F(p)$ to

$$F(p) = F(x_1\|p_1\|, \ldots, x_{10}\|p_{10}\|) = \tilde{F}(x).$$

The partial derivative of $\tilde{F}$ with respect to x_i, obtained using the chain rule

$$\frac{\partial \tilde{F}}{\partial x_i} = \frac{\partial F}{\partial p_i} \cdot \frac{\partial p_i}{\partial x_i} = \|p_i\| \frac{\partial F}{\partial p_i},$$

measures the sensitivity relative to the respective scale. Without normalization, a direct comparison of their derivatives would be less reasonable. This approach corresponds to the logarithmic differential and thus to the sensitivity in terms of elasticity theory, i.e., the percentage change in F for a percentage change in p_i.

549 DEFINITION 3.2. *We define the sensitivity κ_j of the forward operator with respect*
550 *to a certain parameter $x_j,\ j \in \{1,\dots,n\}$, as*
(3.4)

$$\{\kappa_{j,\omega}(x)\}_{\omega\in\mathcal{W}} := \left\{ \left| \frac{\partial \tilde{F}_\omega(x)}{\partial x_j} \right| \right\}_{\omega\in\mathcal{W}} \quad \textit{with} \quad \kappa := \begin{pmatrix} \kappa_{1,1} & \cdots & \kappa_{1,\omega_{|\mathcal{W}|}} \\ \vdots & \ddots & \vdots \\ \kappa_{n,1} & \cdots & \kappa_{n,\omega_{|\mathcal{W}|}} \end{pmatrix} \in \mathbb{R}^{n\times|\mathcal{W}|}$$

552 *being the sensitivity matrix, and the total sensitivity V_j of the forward operator with*
553 *respect to a certain parameter $x_j,\ j \in \{1,\dots,n\}$, as*

$$V_j(x) := \sum_{\omega\in\mathcal{W}} \kappa_{j,\omega}(x). \tag{3.5}$$

555 *Furthermore, we define the cross-sensitivity $\xi^{j,l}$ of the forward operator with respect*
556 *to the parameter x_j and $x_l,\ j,l \in \{1,\dots,n\},\ j \neq l$, as*

$$\xi^{j,l}(x) := \sum_{\omega\in\mathcal{W}} \left| \frac{\partial}{\partial x_l} \left(\frac{\partial \tilde{F}_\omega(x)}{\partial x_j} \right) \right|. \tag{3.6}$$

558 A high value of the cross-sensitivity $\xi^{j,l}$ indicates that a change in parameter x_l
559 significantly alters the sensitivity of the model to parameter x_j. In the context of
560 optimization, this means that the gradient with respect to x_j is highly dependent on
561 the value of x_l. The pairwise parameter coupling via cross-sensitivities is encoded in
562 the strictly upper triangular matrix

$$\xi(x) = \begin{pmatrix} 0 & \xi^{1,2} & \xi^{1,3} & \dots & \xi^{1,n} \\ 0 & 0 & \xi^{2,3} & \dots & \xi^{2,n} \\ \vdots & \vdots & \ddots & \ddots & \vdots \\ 0 & 0 & \cdots & 0 & \xi^{n-1,n} \\ 0 & 0 & \cdots & 0 & 0 \end{pmatrix}, \tag{3.7}$$

564 where each entry $\xi^{j,l},\ j < l$, quantifies the cross-sensitivity between parameters x_j
565 and x_l. It can be understood as a structural measure of pairwise interactions be-
566 tween model parameters. Specifically, off-diagonal entries $\xi^{j,l},\ j < l$, quantify the
567 cross-sensitivity between parameters x_j and x_l and hence the parameter coupling and
568 interaction. Due to the assumed smoothness, $\xi(x)$ could also be chosen as symmetric
569 matrix. However, the strictly upper triangular representation of $\xi(x)$ is motivated to
570 avoid redundancy in encoding pairwise parameter interactions. Consistent with the
571 strictly upper triangular representation in (3.7), we set $\xi^{j,l}(x) := 0$ for $j \geq l$. To
572 capture directional sensitivity interactions that go beyond pairwise effects, we intro-
573 duce a scalar, curvature-based measure derived from second-order derivatives of the
574 objective function. For each block b_k, we define the intra-block roughness measure of
575 the gradient

$$\hat{\xi}_{b_k}(x) := \frac{1}{V_{b_k}(x)} \sum_{i,j\in b_k} \xi^{i,j} \quad \text{for } k \in \{1,\cdots,m\}, \text{ where}$$

$$V_{b_k}(x) := \sum_{i\in b_k} V_i(x) \quad \text{for } k \in \{1,\cdots,m\}$$

denotes the total first-order sensitivity of block b_k, which is reasonably assumed to be strictly positive for every b_k, otherwise the parameters in b_k would have no influence on the forward operator at all. Therefore, $\hat{\xi}_{b_k}$ measures the rate at which the gradient of the objective function changes along the directions in b_k, normalized by first-order sensitivity in that direction. High values of $\hat{\xi}_{b_k}(x)$ identify directions exhibiting strong non-linearity or potential numerical instability. Consequently, one may see this quantity as local condition number. The intra-block roughness measure $\hat{\xi}_{b_k}(x)$ can be intuitively understood as an average non-linearity measure of the problem within the parameter subspace defined by block b_k. In the context of BCD, we aim to form parameter groupings that have a stable gradient in terms of roughness and are externally as decoupled as possible, where the latter is certainly more important. We consider a partition into non-trivial, disjoint blocks. Let the set of all admissible m-partitions be defined as

$$\mathcal{P}_m := \left\{ P \subset \mathcal{P}(\{1,\dots,n\}) : \dot{\cup}_{i=1}^{m} b_{\iota_i} = \{1,\dots,n\} \right\}, \tag{3.8}$$

where $\mathcal{P}$ denotes the power set. To guarantee external decoupling, we define the inter-block coupling as the total cross-sensitivity across two blocks in a specific $P \in \mathcal{P}_m$ as

$$\xi_{b_k,b_l}(x) := \sum_{i \in b_k} \sum_{j \in b_l} \xi^{i,j}(x). \tag{3.9}$$

To determine optimal parameter blocks, we minimize a composite objective function that combines inter-block cross-sensitivity with the intra-block roughness measure,

$$\min_{P \in \mathcal{P}_m} w_1 \sum_{b_k \in P} \hat{\xi}_{b_k}(x) + w_2 \sum_{b_k \in P} \sum_{\substack{b_l \in P \\ b_l \neq b_k}} \xi_{b_k,b_l}(x), \tag{3.10}$$

where $w_1, w_2 \in \mathbb{R}_{\geq 0}$ are pre-defined weights representing the trade-off between interaction across the blocks and the roughness within each block. It is reasonable to emphasize the cross-sensitivity between blocks, i.e., we choose weights $w_1, w_2 \in [0,1]$ with $w_1 \ll w_2$ and $w_1 = 1 - w_2$. Minimizing the first term ensures that blocks are composed of parameters with small roughness in the gradient, i.e., with mildly non-linear sensitivity structures. The second term penalizes the interaction across the blocks, i.e., minimal coupling. Once blocks are formed, the total first-order sensitivity of the blocks may guide the prioritization of block updates during the BCD update, for instance by selecting the block with highest total first-order sensitivity first. Since $|\mathcal{P}_m|$ denotes the number of ways to partition n parameters into m blocks, it grows rapidly with n and m. It is related to the Stirling numbers of the second kind as it can be seen as general graph partitioning problem of a complete weighted graph. Hence, it is useful to deal with small dimensions, where exhaustive enumeration can be used. For larger dimensions greedy heuristics or relaxation approaches would be necessary. The proposed framework provides an approach to structural decomposition of parameter spaces and offers a refined view of coupling, non-linearity, and stability.

4. Solution of the inverse problem with synthetic data.

4.1. General numerical setting. To perform a valuable analysis of the sensitivities and to solve the inverse problem, it is necessary to implement a suitable numerical model. For this purpose, we use the DO approach, where the problem setting is discretized first. Then, the analysis of the sensitivities and the optimization are

Table 1: Material parameters from [8] used for numerical computation.

Param.	c_{11}	c_{12}	c_{13}	c_{33}	c_{44}	ϵ_{11}	ϵ_{33}	e_{15}	e_{31}	e_{33}
Unit	GPa	GPa	GPa	GPa	GPa	$\mathrm{nF\,m^{-1}}$	$\mathrm{nF\,m^{-1}}$	$\mathrm{C\,m^{-1}}$	$\mathrm{C\,m^{-1}}$	$\mathrm{C\,m^{-1}}$
Value	151.4	132.7	83.6	128.8	25.9	2.7	5.5	9.4	-5.2	13.9

performed within this finite-dimensional setting. Specifically, the spatial discretization is realized using a classical *finite element method* (FEM) implemented in the FEM tool FEniCS [1] (dolfin version 2019.2.0.dev0). The gradient-based optimization methods including the sensitivity computations described in the previous sections require easy access to first order Fréchet derivatives. To efficiently obtain derivatives as accurate and consistent as possible in a computationally measurable sense [10], we employ AD [11] via the dolfin-adjoint [23] library (version 2019.1.0), which integrates seamlessly with FEniCS. As domain Ω we consider a rectangle with vertices $(2.6, 0)$, $(6.35, 0)$, $(6.35, 1)$, and $(2.6, 1)$, where coordinates are given in mm, which corresponds to a ring-shaped geometry, see Figure 1, with outer radius of 6.35 mm, inner radius of 2.6 mm and thickness of 1 mm. Furthermore, we use $\hat{\phi}^{\mathrm{e}} = 0.03\,\mathrm{V}$ as excitation and perform any numerical realization in kHz. This has the advantage of a better conditioning of the PDE system, as the elastic stiffness parameter is down-scaled with 10^{-6}, the piezoelectric coupling parameter is up-scaled with 10^3 and the permittivity parameter is up-scaled with 10^{12}, yielding that the magnitudes of the material parameters differ significantly less. The material parameters selected for the FEM simulations are presented in Table 1. The damping parameters $\alpha = 37.8\,\mathrm{ms^{-1}}$ and $\beta = 42\,\mathrm{fs}$ as given in [8] are used throughout the remainder of this paper. The element size h and the polynomial order g are the key factors in determining the frequency at which this configuration is suitable, and the numerical deviations that are to be expected above that frequency. According to [13], it is possible to specify a frequency

$$f < \left(g + \frac{1}{2}\right) \frac{1}{\pi h} \sqrt{\frac{c^{\mathrm{D}}}{\rho}} \tag{4.1}$$

for which the model delivers satisfactory results. A comparison of the numerical deviation of the results and the computational time indicates that an element size of $h = 150\,\mu\mathrm{m}$ and a polynomial order of $g = 3$ yield sufficiently reasonable simulation outcomes. Using inequality (4.1), $c^{\mathrm{D}} = 170\,\mathrm{GPa}$ and $\rho = 7850\,\mathrm{kg\,m^{-3}}$ for a PIC181 piezoceramic [25], this results in a frequency of $f < 34.56\,\mathrm{MHz}$, which suits the assumed frequency range. Consequently, this configuration is employed for the subsequent computations. Furthermore, specifying the Dirichlet lift function $\hat{\chi}$ in the system (2.4) - (2.7) is not necessary and can be avoided in practice, as it is possible to directly implement mixed Dirichlet conditions in FEniCS.

4.2. Sensitivity analysis. This section details the sensitivity analysis, motivating the sensitivity-driven block partitioning strategy for the BCD algorithm that follows. From [8] conclusions can be drawn about the reasonable frequency domains for the inverse problem. Therein it is emphasized that the range between the first radial resonance and the capacitive range between the first and second thickness resonance is particularly suitable for parameter identification. Hence, we will use

$$\mathcal{F}_{\mathrm{g}} := \{f \in \mathbb{N} :\ f \equiv 0 \bmod 5,\ f \leq 6000\}, \quad \mathcal{W}_{\mathrm{g}} := \{\omega = 2\pi f \in \mathbb{R}^+ : f \in \mathcal{F}_g\}. \tag{4.2}$$

To effectively visualize and compare the sensitivities, we will scale the sensitivities on the one hand, with normalization of one sensitivity for all angular frequency points

after the respective (row-wise) maximum and, on the other hand, of all sensitivities for one angular frequency point after the respective (column-wise) maximum. These two normalization schemes that scale the sensitivity matrix result in the scaled matrices

$$\kappa^{\mathrm{rm}} := \begin{pmatrix} \frac{\kappa_{1,1}}{\max_{\omega\in\mathcal{W}_{\mathrm{g}}} \kappa_{1,\omega}} & \cdots & \frac{\kappa_{1,\omega_{|\mathcal{W}|}}}{\max_{\omega\in\mathcal{W}_{\mathrm{g}}} \kappa_{1,\omega}} \\ \vdots & \ddots & \vdots \\ \frac{\kappa_{10,1}}{\max_{\omega\in\mathcal{W}_{\mathrm{g}}} \kappa_{10,\omega}} & \cdots & \frac{\kappa_{10,\omega_{|\mathcal{W}|}}}{\max_{\omega\in\mathcal{W}_{\mathrm{g}}} \kappa_{10,\omega}} \end{pmatrix}, \quad \kappa^{\mathrm{cm}} := \begin{pmatrix} \frac{\kappa_{1,1}}{\max_{j} \kappa_{j,1}} & \cdots & \frac{\kappa_{1,\omega_{|\mathcal{W}|}}}{\max_{j} \kappa_{j,\omega_{|\mathcal{W}|}}} \\ \vdots & \ddots & \vdots \\ \frac{\kappa_{10,1}}{\max_{j} \kappa_{j,1}} & \cdots & \frac{\kappa_{10,\omega_{|\mathcal{W}|}}}{\max_{j} \kappa_{j,\omega_{|\mathcal{W}|}}} \end{pmatrix}. \tag{4.3}$$

Ideally, all partial sensitivities would be similar and close to one, but this is by no means realistic in practical applications, as the sensitivities depend, among other things, on the overall geometry of the ceramic itself, which will not be changed. One can try to increase sensitivities either via a sensitivity optimization or via optimal experiment design of electrode configurations, see [15]. The BCD approach is an alternative that does not change, but provides better handling of sensitivities. For the subsequent sensitivity results, we used the parameters in Table 1, chose the angular frequency grid $\mathcal{W}_{\mathrm{g}}$ defined in (4.2) and used AD for first- and second-order sensitivity computations. In the top row of Figure 2 we see the illustration of the matrices in (4.3), where the black points indicate those sensitivities $\kappa_{j,\omega}$ over $\mathcal{W}_{\mathrm{g}}$ which are higher than 90 % of $\max_{\omega\in\mathcal{W}_{\mathrm{g}}} \kappa_{j,\omega}$ for each $j \in \{1,\dots,10\}$. The row-wise normalization (κ^{rm}, top left in Figure 2) highlights the frequency-dependent profile of each parameter's sensitivity relative to its own maximum. For example, c_{11} and c_{33} exhibit sharp peaks near the material's resonance frequencies. Conversely, the column-wise normalization (κ^{cm}, top right in Figure 2) illustrates which parameter dominates at a specific frequency. The existing approaches to group parameters enforce to categorize them in similar frequency domain regions. This means that parameters are grouped

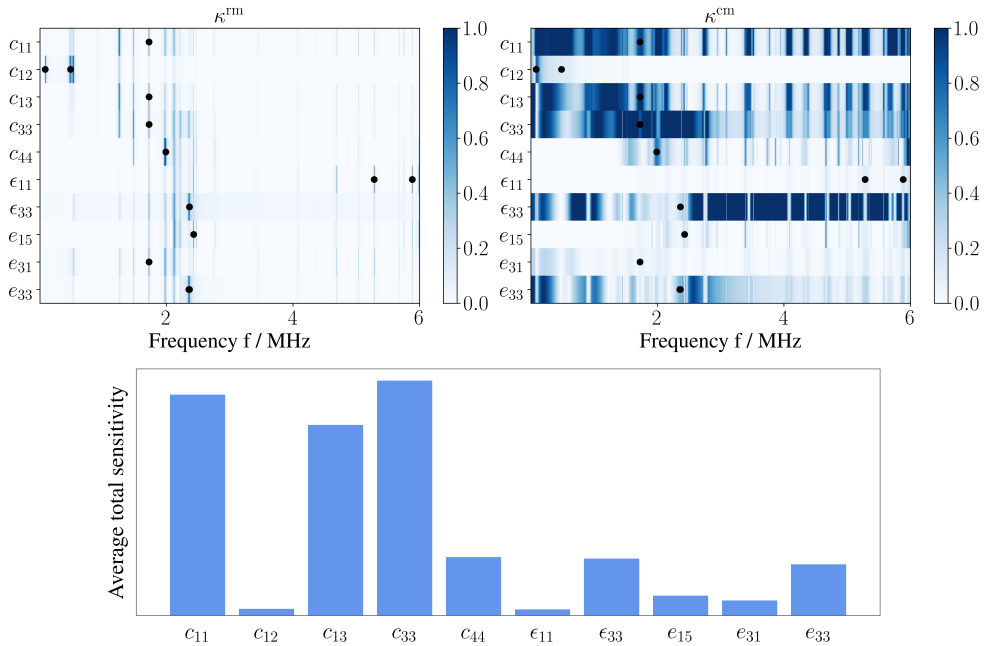


Figure 2: Top row: Row-wise and column-wise normalized sensitivities κ^{rm} and κ^{cm} with respect to the parameters in Table 1 on $\mathcal{W}_{\mathrm{g}}$; Bottom row: Total average sensitivities of the forward operator with respect to the parameters in Table 1 on $\mathcal{W}_{\mathrm{g}}$.

together, which have high sensitivity at a specific frequency range and optimize them on that range, while keeping them fixed at other ranges, see [7]. Nevertheless, the interaction between those parameters in a specific range can be high. We do not follow that approach of domain splitting, as we emphasize reducing the inter cross-sensitivities and use a BCD approach instead of a pure coordinate descent approach as in [8]. As mentioned before, the sensitivities of the forward operator in piezoelectric inverse parameter identification problems can vary strongly, which is illustrated also in the bottom row of Figure 2. Since the cross-sensitivity analysis is especially useful for the block choice in the subsequent inverse problem, we assume the same numerical configurations. Specifically, we use the same spatial mesh, initial parameters and angular frequency domain grid for the solution to the inverse problem (2.16) and for the solution to the combinatorial block choice problem (3.9). We specify as initial guess p_0 the parameters in Table 1 with 5% overestimation. To dampen any amplification of the discrepancy in sensitivities by the forward operator we select a suitable angular frequency range, see [17]. From the top row of Figure 2, conclusions can be drawn about reasonable frequency domains for the inverse problem. Due to the small sensitivities of the forward operator with respect to c_{12} and ϵ_{11}, we use a fine angular frequency grid in areas where the forward operator is more sensitive to those parameters and in resonance areas. In the other parts of the angular frequency domain we use a coarse grid. Hence, with the frequency domains

$$\mathcal{F}_1 := \{f \in [38, 2600) : f \equiv 0 \bmod 3\},\ \mathcal{F}_2 := \{f \in [2600, 4500) : f \equiv 0 \bmod 20\},$$
$$\mathcal{F}_3 := \{f \in [4500, 6000] : f \equiv 0 \bmod 3\},$$

where the intervals are understood as subsets of $\mathbb{N}$, we consider

$$\mathcal{W}_\mathrm{a} := \{\omega = 2\pi f \in \mathbb{R}^+ :\ f \in \mathcal{F}_1 \cup \mathcal{F}_2 \cup \mathcal{F}_3\} \tag{4.4}$$

as angular frequency domain. This adaptive selection concentrates computational effort in angular frequency regions rich with information, while sparsely sampling regions where the model is less sensitive. This can be viewed as a form of a-posteriori experimental design, optimizing the data used for the inversion rather than the physical experiment itself. Furthermore, this results in the advantage of less computations in the sensitivity analysis as the cardinality of the angular frequency domain became smaller. With this approach we obtain the cross-sensitivities, c.f. identity (3.7), for all parameters as shown in Figure 3, illustrating clearly the disparity in cross-sensitivities.

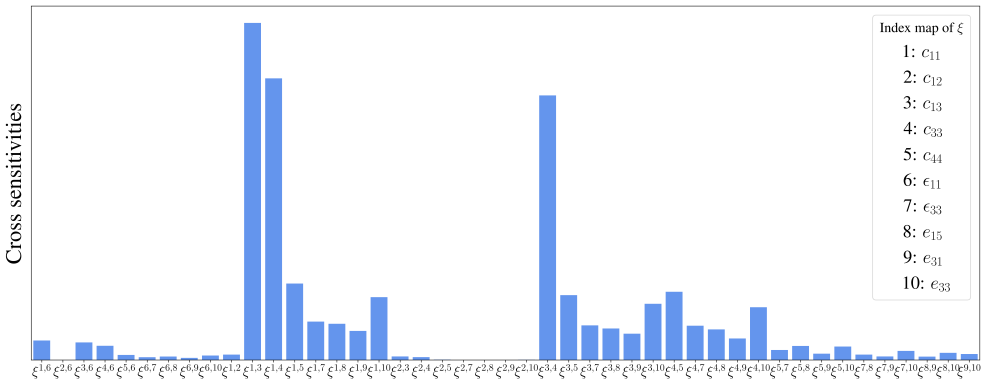


Figure 3: Total cross-sensitivities of the forward operator with parameters in Table 1 and 5% overestimation on $\mathcal{W}_\mathrm{a}$.

The bars corresponding to pairs like $(c_{11},\ c_{13})$ and $(c_{11},\ c_{33})$ represent strong interactions where a change in one parameter drastically alters the gradient with respect to the other. Unadapted optimization algorithms could struggle with such a landscape, as the search direction would be compromised by these conflicting influences. Since we want to reconstruct $n = 10$ material parameters, we have $\mathcal{I} = \{1, 2, \ldots, 10\}$ as the index set of parameters for a fixed $\theta \in \Theta$ in our concrete application. As detailed above, we will use a cyclic BCD-GRSE method and consider a bipartition, i.e., $m = 2$, into two non-trivial, mutually disjoint blocks. Blocks of size one contain no pairwise parameter interactions and would therefore be artificially favored by the block partitioning objective. Hence, we consider

$$b_1 \subset \mathcal{I}, \quad b_2 = \mathcal{I} \setminus b_1, \quad \text{with} \quad 2 \leq |b_1|, |b_2| \leq 8. \tag{4.5}$$

Then, the problem of determining optimal parameter blocks simplifies to

$$\min_{\substack{b_1 \subset \mathcal{I} \\ 2 \leq |b_1| \leq 8}} \ w_1 \left(\hat{\xi}_{b_1}(x) + \hat{\xi}_{b_2}(x) \right) + w_2 \cdot \xi_{b_1, b_2}(x). \tag{4.6}$$

Since $n = 10$ and $m = 2$, we use exhaustive enumeration to solve problem (4.6), where we chose $w_1 = 0.1$ and $w_2 = 0.9$, resulting in the partition

$$b_1 = \{c_{11},\ c_{13},\ c_{33},\ c_{44},\ \epsilon_{33},\ e_{15},\ e_{31},\ e_{33}\}, \quad b_2 = \{c_{12},\ \epsilon_{11}\}.$$

Computing the total first-order sensitivity of each block suggests that we prioritize b_1. This partitioning is also supported by the intuitive approach of combining the two parameters with the lowest overall sensitivity (c_{12} and ϵ_{11}) into a separate block. However, this intuitive strategy would not necessarily be effective, as inter-block correlations may still be high. The advantage of our approach is that we are able to reasonably conclude that the parameter blocks exhibit small interaction and the dominant parameters are isolated.

4.3. Solution to the simulation-based inverse problem. To validate the performance of the BCD-GRSE algorithm and the effectiveness of the sensitivity-based block partitioning strategy, we first conduct a numerical experiment using synthetic data. To generate the noisy data y^δ we contaminate the exact simulated data $Q_\omega^\theta(p, z)$, generated according to the parameters in Table 1, additively with uniformly

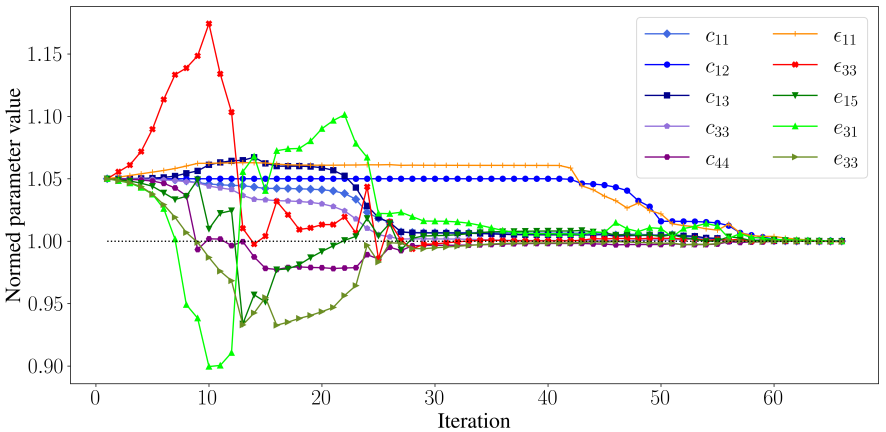


Figure 4: BCD-GRSE parameter identification from simulated noisy data.

distributed random noise with a noise level of 2%, i.e., $\tilde{y}^\delta_\omega = (1+\nu_\omega)\left\|Q^\theta_\omega(p,z)\right\|_{\mathbb{C}}$ with $\nu_\omega \sim \mathcal{U}(-0.02, 0.02)$ and subsequently the logarithmic transformation is applied to obtain y^δ. As initial guess p_0 we used the parameters in Table 1 with 5% overestimation. Additionally, we performed numerical tests using a 5% underestimated initial guess, which yielded similar convergence results. We employ the hyperparameters $\mu = 0.5$, $\tau_0^1 = \tau_0^2 = 10^{-3}$, $\sigma = 4$, $c = a = 10^{-2}$ and $\eta^1 = 5\eta^2$, $\eta^2 = 1.45 \cdot 10^{-5}$. For improved stability, the regularization parameter of the second block was reduced when the norm of the first-block update dropped below 1 for the first time. Here, μ is the decay factor and σ is the growth factor of the regularization parameters for each block, see [19], and c, a refer to c, p in [19]. As initial Quasi-Newton matrices for each block we use $F''(p_0)^*\left(F(p_0) - y^\delta\right)$, where $F''(p_0)$ is computed via AD. Figure 4 shows the parameter identification performance of the BCD-GRSE method. For the sake of better visualization, the reconstructed parameter values have been normalized with the respective true parameter, so that convergence to the value 1 is desired. The reconstruction results in Figure 4 show convergence to the true parameters, even for the least sensitive parameters c_{12} and ϵ_{11}. Throughout the optimization process, every iteration remained feasible. The successful reconstruction from noisy synthetic data provides numerical evidence for the proposed method and validates the sensitivity-driven block decomposition strategy.

5. Application to experimental measurement data.

5.1. Experimental Setup. After the validation of the proposed method using synthetic data, the subsequent step is its application to real measurement data. The behavior of a piezoceramic sample under varying temperature conditions is investigated through the measurement of its electrical impedance at these conditions. The experimental configuration is fundamentally reliant upon a temperature-controlled chamber, in which the sample is securely positioned. This chamber is designed to ensure a constant thermal environment for the specimen during the impedance measurement. Temperature regulation is achieved via a precise thermostat system (*Magio MS-310F, Julabo, Germany*). At each temperature point θ within the temperature range $\Theta := \{\theta \in [25, 85] \cap \mathbb{N} \mid \theta \equiv 0 \bmod 5\}$, electrical impedance measurements are conducted using an impedance analyzer (*E4990A, Keysight Technologies, USA*). Ventilation is implemented to ensure uniform temperature distribution within the chamber, thereby minimizing temperature gradients across the sample. Both the thermostat and the impedance analyzer are computer-controlled, enabling automated measurements to be conducted across the entire temperature range. A sufficient time period of half an hour is implemented to allow the sample to reach thermal equilibrium with the chamber. The examined specimen is a PIC181 (*PI Ceramic, Germany*) annular piezoelectric ceramic with dimensions that correspond to those previously described in Section 4 and shown in Figure 1. As the data measured at each temperature is a vector consisting of absolute values of the impedance, i.e.,

$$\left\|Z^\theta_\omega(p,z)\right\|_{\mathbb{C}} := \left\| \frac{-\hat{\phi}^{\mathrm{e}} Q^{\theta,i}_\omega(p,z)}{\omega \|Q^\theta_\omega(p,z)\|^2_{\mathbb{C}}} + i \frac{-\hat{\phi}^{\mathrm{e}} Q^{\theta,r}_\omega(p,z)}{\omega \|Q^\theta_\omega(p,z)\|^2_{\mathbb{C}}} \right\|_{\mathbb{C}} = \frac{\hat{\phi}^{\mathrm{e}}}{\omega \|Q^\theta_\omega(p,z)\|_{\mathbb{C}}},$$

we equivalently convert it according to the forward operator via

$$\left\|Q^\theta_\omega(p,z)\right\|_{\mathbb{C}} = \frac{\hat{\phi}^{\mathrm{e}}}{\omega \|Z^\theta_\omega(p,z)\|_{\mathbb{C}}} \quad \text{resulting in} \quad y^\delta_\omega := \log\left(\frac{\hat{\phi}^{\mathrm{e}}}{\omega \|Z^\theta_\omega\|^{\mathrm{meas}}_{\mathbb{C}}}\right).$$

Table 2: Results of the parameter identification for each $\theta \in \Theta$ based on real measurement data applying the BCD-GRSE algorithm.

θ \ p_j	c_{11}	c_{12}	c_{13}	c_{33}	c_{44}	ϵ_{11}	ϵ_{33}	e_{15}	e_{31}	e_{33}
25	140.866	72.667	78.466	129.929	28.213	8.595	5.580	11.673	-5.468	14.102
30	140.997	73.131	78.539	130.023	28.252	8.912	5.651	11.825	-5.473	14.238
35	141.197	73.451	78.668	130.034	28.227	8.741	5.723	11.788	-5.473	14.356
40	141.456	73.958	78.816	130.027	28.203	8.582	5.811	11.761	-5.495	14.467
45	141.579	74.177	78.883	130.044	28.207	8.543	5.890	11.789	-5.519	14.548
50	141.527	74.104	78.865	130.142	28.206	8.557	5.990	11.811	-5.576	14.625
55	141.244	73.550	78.688	130.193	28.233	8.585	6.087	11.819	-5.626	14.729
60	141.076	73.294	78.556	130.234	28.319	8.923	6.184	11.971	-5.656	14.871
65	141.252	73.786	78.530	130.232	28.642	10.502	6.293	12.711	-5.581	15.097
70	141.513	74.344	78.582	130.179	28.608	10.246	6.376	12.598	-5.567	15.213
75	141.761	74.853	78.680	130.128	28.498	9.575	6.480	12.334	-5.622	15.305
80	141.260	73.665	78.430	130.300	28.608	10.033	6.578	12.503	-5.680	15.402
85	141.269	73.872	78.384	130.432	28.728	10.649	6.698	12.762	-5.711	15.554

5.2. Results based on measurement data. The angular frequency grid for the reconstruction is chosen as in Section 4. Then, for each fixed temperature we have to reconstruct a different set of material parameters. We start by reconstructing the material parameters at 25 °C, where we use the parameters given in Table 1 as initial parameters. Since the material properties at a given temperature are assumed to be independent of the properties at other temperatures, the inverse problem can be solved independently for all remaining temperatures. This allows the application of a trivial parallelization of the characterization process. Consequently, after obtaining the results for 25 °C, given in the first row of Table 2, we use those parameters as initial parameters for all remaining $\theta \in \Theta$. We expect on the one hand that this approach yields a better initial guess and on the other hand significantly faster convergence. Furthermore, we employed the same hyperparameters as in Subsection 4.3 and used $F''(p_0)^* \left(F(p_0) - y^\delta\right)$, where $F''(p_0)$ is computed via AD, as initial QN matrices. Applying the BCD-GRSE algorithm to the experimental data for each temperature $\theta \in \Theta$ yields the values of the parameters as depicted in Table 2, with elasticity parameter components in GPa, piezoelectric coupling parameter components in $\mathrm{C\,m^{-1}}$ and permittivity parameter components in $\mathrm{nF\,m^{-1}}$, rounded to three decimal places. Comparing the data misfit for each temperature achieved by the BCD-GRSE algorithm to the results presented in [9] confirms that our method consistently achieves less than half of the data misfit values of [9], which can be seen in Table 3.

A visual comparison of the measured data, the data generated with the reconstructed parameters using the BCD-GRSE algorithm and the data from [9] showed almost indistinguishable results across the temperature domain. Therefore, we chose results for the representative temperature of 50 °C, illustrated in Figure 5. For better visualization, the first row shows zoomed-in versions of the grey-marked characteristic regions. The reconstructed data corresponding to row 6 in Table 2 align closely with the measurements, validating the accuracy of the identified parameter set presented in Table 2. Notably, the regions containing the most information, i.e., the resonance and anti-resonance areas, show strong agreement between the BCD-GRSE reconstructed data and the measurements. Furthermore, the BCD-GRSE reconstruction provides a substantially better fit to the measurements than the results from [9], as indicated by Table 3, which is particularly visible in these regions. The slight mismatch in

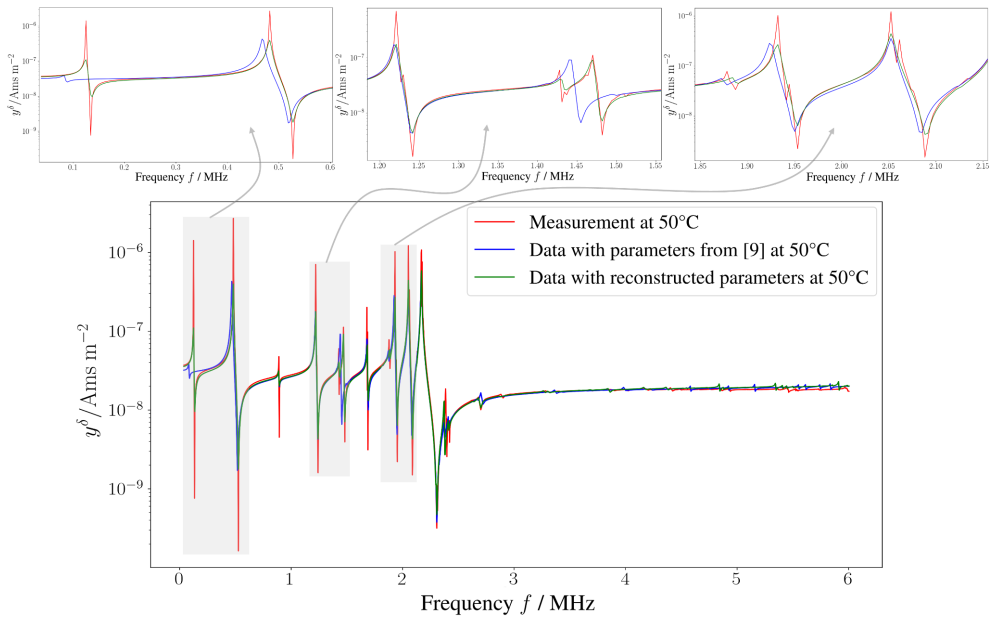


Figure 5: Simulation using reconstructed material parameters compared to simulation using data in [9] and measured data at 50 °C, zooming in on the characteristic resonance and anti-resonance regions.

the peak amplitudes may be attributed to the Rayleigh damping model, which does not fully capture all material loss mechanisms, suggesting the need for further model refinement. To obtain continuous functions representing the temperature dependency of each parameter, we perform an exponential curve approximation on the values in Table 2 and additionally fit a first order polynomial regression model to these values. The advantage of an exponential fit is that we obtain a monotone function, which is a reasonable behavior, while still giving opportunities for possible nonlinearities. Figure 6 shows the identified temperature dependency of the elastic, piezoelectric,

Temperature θ / °C	J_θ using material parameter in [9]	J_θ using material parameter in Table 2	Relative improvement to [9] in %
25	19.976	8.203	58.94%
30	19.463	7.877	59.53%
35	18.770	7.379	60.69%
40	17.904	6.812	61.95%
45	17.035	6.373	62.59%
50	16.821	6.379	62.08%
55	17.122	6.614	61.37%
60	16.863	6.459	61.70%
65	16.299	5.845	64.14%
70	15.900	5.435	65.82%
75	16.130	5.895	63.45%
80	15.653	5.872	62.49%
85	15.771	5.737	63.62%

Table 3: Data misfit values using reconstructed material parameters in Table 2 compared to data misfit values using material parameters of [9] and the relative improvement to [9].

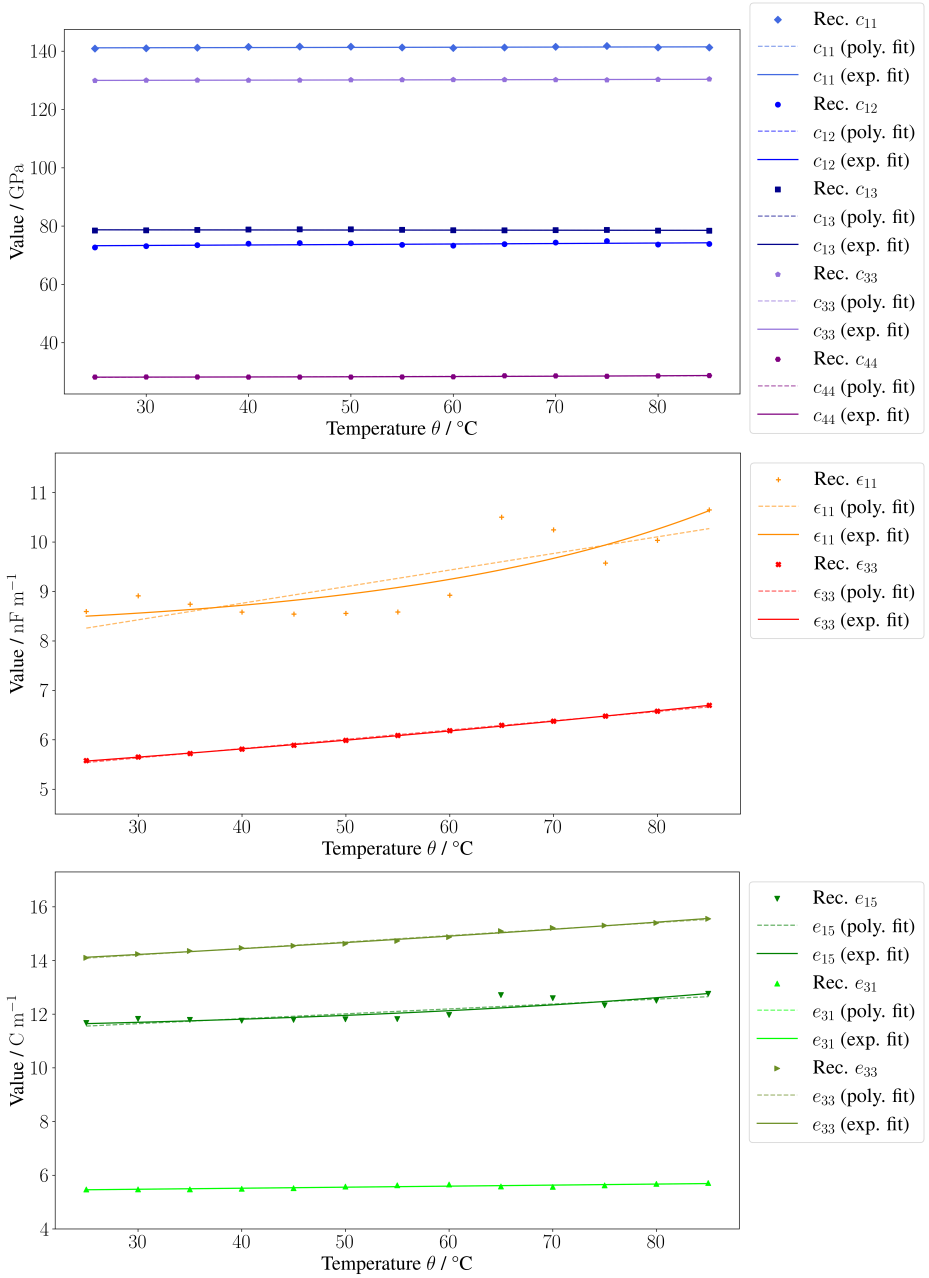


Figure 6: Reconstructed temperature-dependent material behavior of c^{E}, ϵ^{S} and e with first order polynomial fit (dashed lines) and exponential fit (solid lines).

and dielectric parameters, respectively. The points represent the discrete values from Table 2, the solid lines represent the exponential curve fit and the dashed lines the fitted polynomial functions of first order. The identified parameters in Figure 6 show clear trends with increasing temperature. The elastic stiffness parameters (top in Figure 6) exhibit a nearly constant behavior with a negligible slope as temperature rises. Conversely, the permittivity (middle in Figure 6) and piezoelectric coupling (bottom in Figure 6) components demonstrate significant temperature dependence.

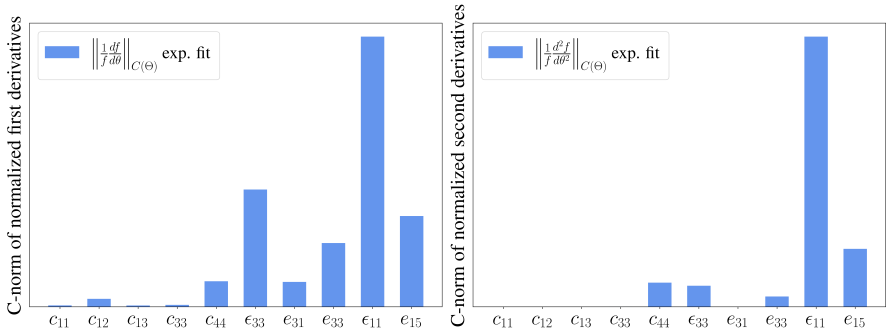


Figure 7: C-norm of normalized first and second derivatives of the exponential parameter functions.

A pronounced linear increase is observed for the permittivity parameter $\epsilon_{33}(\theta)$. Similarly, the piezoelectric coupling parameter functions $e_{15}(\theta)$, $e_{31}(\theta)$ and $e_{33}(\theta)$ follow a linear trend. However, $\epsilon_{11}(\theta)$ exhibits a non-linear behavior. One factor that could contribute to the non-linearity observed in $\epsilon_{11}(\theta)$ is that the forward operator is least sensitive to this specific parameter. This observation has been made also in previous contributions [8]. To quantify the sensitivity of each parameter function to temperature changes and the non-linearity with respect to temperature, the C-norm (maximum absolute value) of the normalized first and second derivatives of the exponential curves to each parameter function are illustrated in Figure 7. The C-norm of the normalized first derivatives (left in Figure 7) confirms that especially the permittivity and the piezoelectric coupling parameters are sensitive to temperature changes, while the elasticity parameter remains more stable. The right plot in Figure 7 encourages the distinction between seemingly linear and non-linear parameter functions. The seemingly non-linear function $\epsilon_{11}(\theta)$ exhibits high C-norm sensitivity and curvature values, which supports the hypothesis that the observed non-linearity arises from a combination of the low sensitivity and potential physical effects. In contrast, the seemingly linear parameters possess low C-norm curvature values relative to $\epsilon_{11}(\theta)$. Finally, the identified parameter sets for all temperatures satisfy the thermodynamic stability conditions in Definition 2.1, ensuring physical plausibility.

6. Conclusion. In this paper, we presented a framework for identifying temperature-dependent piezoelectric material parameters from charge measurements in the frequency domain. We formulated the forward problem in an axisymmetric environment and analyzed the corresponding inverse problem. To address the strong parameter coupling and sensitivities across very different orders of magnitude, we introduced an algorithmic sensitivity-informed block construction strategy within a block coordinate descent algorithm. The block structure was derived from first- and second-order sensitivity measures, including total sensitivities, cross-sensitivities, and a curvature-based roughness indicator. To address the ill-posedness we used the GRSE method to update each block. Numerical experiments with noisy synthetic data have shown that all piezoelectric material parameters can be reliably reconstructed, including those with very low sensitivity. Finally, we applied the sensitivity-informed BCD-GRSE framework to real charge measurements of a single ring-shaped PIC181 sample over a temperature range of 25 °C to 85 °C. The match between the simulation with the reconstructed material parameters and the measurement data has been improved and is satisfactorily accurate. In summary, the determined material parameters represent plausible solutions to the inverse problem and can thus be con-

sidered representative of the real ceramic in the sense of the applied FEM model. As a result, the proposed approach provides a robust and theoretically sound method for determining piezoelectric parameters under realistic measurement conditions.

Acknowledgments. The authors thank the Deutsche Forschungsgemeinschaft (DFG, German Research Foundation) for financial support within the research group 5208 NEPTUN (444955436). The work on this paper was partly funded by the DFG under Germany's Excellence Strategy – The Berlin Mathematics Research Center MATH+ (EXC-2046/1, EXC-2046/2, project ID: 390685689).

REFERENCES

[1] M. Alnæs, J. Blechta, J. Hake, A. Johansson, B. Kehlet, A. Logg, C. Richardson, J. Ring, M. E. Rognes, and G. N. Wells, *The FEniCS project version 1.5*, Archive of Numerical Software, 3 (2015).
[2] F. Anderl and M. Mayle, *Sensitivity analysis of piezoelectric material parameters using Sobol indices*, tm - Technisches Messen, 92 (2025), pp. 234–242.
[3] O. Burghardt, P. G. N. R. Gauger, T. K. R. Palacios, and T. Economon, *Coupled discrete adjoints for multiphysics in su2*, AIAA 2020-3139, (2020).
[4] L. Claes, K. Koch, O. Friesen, and L. Meihost, *Machine learning-supported inverse measurement procedure for broadband, temperature dependent piezoelectric material parameters*, Acta Acustica, 9 (2025).
[5] N. Feldmann, B. Jurgelucks, L. Claes, V. Schulze, B. Henning, and A. Walther, *An inverse approach to the characterisation of material parameters of piezoelectric discs with triple-ring-electrodes*, tm - Technisches Messen, 86 (2019), pp. 59–65.
[6] N. Feldmann, V. Schulze, L. Claes, B. Jurgelucks, L. Meihost, A. Walther, and B. Henning, *Modelling damping in piezoceramics: A comparative study*, tm - Technisches Messen, 88 (2021), pp. 294–302.
[7] N. Feldmann, V. Schulze, L. Claes, B. Jurgelucks, A. Walther, and B. Henning, *Inverse piezoelectric material parameter characterization using a single disc-shaped specimen*, tm - Technisches Messen, 87 (2020), pp. s50–s55.
[8] O. Friesen, L. Claes, N. Feldmann, and B. Henning, *Estimation of piezoelectric material parameters of ring-shaped specimens*, tm - Technisches Messen, (2024).
[9] O. Friesen, L. Claes, C. Scheidemann, N. Feldmann, T. Hemsel, and B. Henning, *Estimation of temperature-dependent piezoelectric material parameters using ring-shaped specimens*, Journal of Physics: Conference Series, 2822 (2024), p. 012125.
[10] R. Griesse and A. Walther, *Evaluating gradients in optimal control: continuous adjoints versus automatic differentiation*, J. Optim. Theory Appl., 122 (2004), pp. 63–86.
[11] A. Griewank and A. Walther, *Evaluating derivatives*, SIAM, second edition ed., 2008.
[12] P. Grisvard, *Elliptic Problems in Nonsmooth Domains*, vol. 24 of Monographs and Studies in Mathematics, Pitman Publishing Inc., Boston, MA, 1985. Reprinted by SIAM, 2011, in the Classics in Applied Mathematics series.
[13] A. Hauck, *Higher order finite elements for coupled and anisotropic field problems*, diss., Erlangen, Friedrich-Alexander-Universität Erlangen-Nürnberg , 2016.
[14] B. Jurgelucks, *Increased sensitivity in parameter identification problems for piezoelectrics*, diss., Paderborn University, 2019.
[15] B. Jurgelucks, L. Claes, A. Walther, and B. Henning, *Optimization of triple-ring electrodes on piezoceramic transducers using algorithmic differentiation*, Optimization Methods and Software, 33 (2018), pp. 868–888.
[16] C. Kanzow and D. Steck, *Regularization of limited memory quasi-Newton methods for large-scale nonconvex minimization*, Math. Progr. Comp., 15 (2023), pp. 417–444.
[17] R. Kuess, O. Friesen, B. Henning, and A. Walther, *Identification of temperature-dependent material parameter functions in piezoelectricity*, in Proceeding of 2025 ICU, Paderborn, Germany, AMA Service GmbH, 2025, pp. 134–137.
[18] R. Kuess, D. Walter, and A. Walther, *Modelling and analysis of an inverse parameter identification problem in piezoelectricity*. Optimization Online, 2026, https://optimization-online.org/?p=33654.
[19] R. Kuess and A. Walther, *On regularized structure-exploiting quasi-newton methods for inverse problems*, Optimization Methods and Software, 0 (2026), pp. 1–35, https://doi.org/10.1080/10556788.2026.2686965.

[20] T. Lahmer, *Forward and inverse problems in piezoelectricity*, diss., Friedrich-Alexander-Universität Erlangen-Nürnberg (FAU), 2008.
[21] T. Lahmer, J. Ilg, and R. Lerch, *Variance-based sensitivity analyses of piezoelectric models*, Computer Modeling in Engineering & Sciences, 106 (2015), pp. 105–126.
[22] W. McLean, *Strongly Elliptic Systems and Boundary Integral Equations*, Cambridge University Press, 2000.
[23] S. Mitusch, S. Funke, and J. Dokken, *dolfin-adjoint 2018.1: automated adjoints for FEniCS and Firedrake*, Journal of Open Source Software, 4 (2019), p. 1292.
[24] J. Nutini, I. Laradji, and M. Schmidt, *Let's make block coordinate descent converge faster: faster greedy rules, message-passing, active-set complexity, and superlinear convergence*, J. Mach. Learn. Res., 23 (2022).
[25] PI Ceramic GmbH, *Material data: Specific parameters of standard materials*, 8 2025.
[26] S. Wright, *Coordinate descent algorithms*, Math. Programming, 151 (2015), pp. 3–34.